Impacts of a Porous Surface on Flame Acceleration

by

Ariyanna Kresnyak

A thesis

presented to the University of Waterloo

in fulfillment of the

thesis requirement for the degree of

Master of Applied Science

in

Mechatronics and Mechanical Engineering

Waterloo, Ontario, Canada, 2026

© Ariyanna Kresnyak 2026

Author's Declaration

I hereby declare that I am the sole author of this thesis. This is a true copy of the thesis, including any required final revisions, as accepted by my examiners.

I understand that my thesis may be made electronically available to the public.

Abstract

Deflagration-to-detonation transition (DDT) is a critical phenomenon in the development of detonation-based propulsion systems and in industrial gas safety. Recent experimental investigations by Jiang et al. [41] and Lin et al. [62] demonstrated that porous copper foam integrated into the walls of a square combustion channel reduced the detonation onset distance of a stoichiometric ethylene-oxygen mixture. Understanding the mechanisms responsible for this behaviour remains incomplete.

This work investigates the influence of a porous boundary on flame acceleration and pressure-field development through direct numerical simulation using the compressible reacting-flow solver PeleC. Simulations were performed for a stoichiometric ethylene-oxygen mixture within a 30 mm $\times$ 30 mm square tube. The porous medium was represented using a simplified custom boundary condition consisting of evenly spaced circular outlet pores. This representation was intentionally designed to isolate surface-level mass and flow interactions while excluding combustion and transport within the internal pore structure. Post-processing techniques were developed to quantify flame propagation, shock formation, pressure-field evolution, and transport through the porous boundary.

Equal-resolution comparison of the smooth-wall and porous simulations demonstrated no measurable reduction in bulk flame velocity over the available simulation interval. However, the porous boundary substantially altered pressure-wave development. Shock formation was delayed by approximately 56 μs relative to the smooth-wall simulation while occurring at a similar axial location, indicating that the porous boundary primarily influenced the rate of pressure-wave buildup. Interaction between the developing pressure

field and porous boundary began prior to direct flame interaction with the pores, while mass and kinetic-energy transport increased substantially following arrival of the flame and high-pressure products. Velocity-field analysis additionally identified a reversal in transverse near-wall flow that provides a potential coupling mechanism between the bulk flame and processes occurring within the porous structure.

The results demonstrate that, under the simplifying assumption of representing the porous medium as surface-level outlet pores, the experimentally observed enhancement in flame acceleration is not reproduced. The simulations instead demonstrate pressure-wave attenuation and delayed shock development while retaining similar bulk flame propagation at equal resolution. These findings indicate that physical processes excluded by the simplified boundary representation, particularly combustion and flow transport within the porous volume, may be important to reproducing the acceleration observed experimentally.

Acknowledgements

This work is completed with appreciation for, and thanks to, Adam Trumpour and Jean-Pierre Hickey who have created community and opportunity in regard to the pursuit of Canadian rocket science.

Additional recognition is given to Derek Hayden. Support from advisors and those established in their careers is significant, but it does little to fight impostor syndrome the way that support from your peers does. The support your friendship has provided made it easier to continue doing the work when I held nothing but doubt.

Dedication

This work is dedicated to Marielle Duplak who built her own strength to support my academic passions. Together we are a team stronger than the sum of its parts. I have carried her through her challenges, and in the pursuit of this work she has carried me through mine.

Table of Contents

Author's Declaration ii

Abstract iii

Acknowledgements v

Dedication vi

List of Figures ix

List of Tables xii

1 Introduction 1

1.1 Deflagration vs Detonation 1

1.2 Application of Detonations 4

1.3 Initiation of Detonation 9

2 Literature Review 18

2.1 Historical Development of DDT Mechanisms 18

2.2 Experimental Investigation of DDT 21

2.3 Numerical Approaches for DDT Simulation 27

2.4 Motivation 31

3 Methodology **34**
3.1 Numerical Framework . . . 35
3.2 Governing Equations . . . 37
3.3 Computational Domain and Geometry . . . 38
3.4 Mesh, Boundary and Initial Conditions . . . 39
3.5 Post-processing and Data Analysis . . . 43
3.5.1 Extraction of Simulation Data . . . 43
3.5.2 Visualization . . . 44
3.5.3 Flame Front Detection and Flame Speed . . . 45
3.5.4 Shock Wave Detection and Shock Strength . . . 48
3.5.5 Grid Sensitivity Analysis . . . 51

4 Results **54**
4.1 Grid Sensitivity Study . . . 54
4.2 Flame Evolution . . . 57
4.2.1 Null 3AMR Temperature and Pressure Smears . . . 58
4.2.2 10PPI 3AMR Temperature and Pressure Smears . . . 60
4.2.3 10PPI 4AMR Temperature and Pressure Smears . . . 63
4.3 Flame Speed and Propagation . . . 66
4.4 Shock Formation and Pressure Profiles . . . 67
4.5 Notable Observations . . . 71
4.5.1 Temperature drop over pores . . . 71
4.5.2 Pressure ripples emanating from pores . . . 76

5 Discussion **79**

6 Conclusion **87**

References **91**

List of Figures

1.1 Schematic diagram of PDE single cycle. Reprinted from Applied Thermal Engineering, Vol. 244, Y. Li, S. Qi, Q. Jing, L. Zhang, D. Wang, C. Shi, H. Xu, Y. Li, Z. Wu, R. Zhou, The effect of operating frequency and ignition energy on JP-10/PO/aluminum powder multiphase-pulse-detonation-engine, 122758, Copyright (2024), with permission from Elsevier. [59] 7

1.2 Schematic diagram of Standing Wave Detonation Engine. Reprinted from Proceedings of the Combustion Institute, Vol. 34, P. Wolański, Detonative propulsion, 125–158, Copyright (2013), with permission from Elsevier. [107] 8

1.3 Schematic diagram of Rotating Detonation Engine. Reproduced from Shepherd and Kasahara, 2017 [94] 9

1.4 Schema of a gas DDT in a closed tube. Reproduced with permission from McAfee, J. M., "The Deflagration-to-Detonation Transition", Shock Wave Science and Technology Reference Library, Vol. 5: Non-Shock Initiation of Explosives, 2010, Springer Berlin Heidelberg. © 2010 Springer Nature [71] 11

1.5 Schema of vortical amplification. Reproduced with permission from McAfee, J. M., "The Deflagration-to-Detonation Transition", Shock Wave Science and Technology Reference Library, Vol. 5: Non-Shock Initiation of Explosives, 2010, Springer Berlin Heidelberg. © 2010 Springer Nature [71] . . . 12

1.6 Schematic of Detonation Wave Structure. Reprinted from Proceedings of the Combustion Institute, Vol. 38, J. Crane, X. Shi, J. T. Lipkowicz, A. M. Kempf, H. Wang, Geometric modeling and analysis of detonation cellular stability, 3585–3593, Copyright (2021), with permission from Elsevier. [19] 14

1.7 Detonation Wave Cellular Structure. From "Experiments in gasdynamics of explosions," by A. K. Oppenheim and R. I. Soloukhin, 1973, Annual Review of Fluid Mechanics, 5, Copyright 1973 by Annual Reviews. Reprinted with permission. [77] 15

3.1 Boundary conditions 42
3.2 Custom porous wall boundary condition 42
3.3 Slice locations and orientations 45
3.4 Example of flame front detection within the core flow. 47
3.5 Example of flame front detection near the porous wall boundary. 47
3.6 Examples of shock detection of developing pressure wave. Top: Zoomed region of the detected wave, Bottom: row averaged pressure profile 50
3.7 Example of shock detection of formed shock wave. Top: Zoomed region of the detected wave, Bottom: row averaged pressure profile 51

4.1 Bulk flame velocity as a function of flame front position for the 2AMR, 3AMR, and 4AMR simulations 55
4.2 Flame smear from the core Null 3AMR 59
4.3 Pressure smear from the core Null 3AMR 60
4.4 Flame smear from the core 10PPI 3AMR 62
4.5 Pressure smear from the core 10PPI 3AMR 63
4.6 Flame smear from the core 10PPI 4AMR 64
4.7 Pressure smear from the core 10PPI 4AMR 65
4.8 Comparison of the reported experimental flame velocity with the calculated bulk flame velocities of the Null 3AMR, 10PPI 3AMR, and 10PPI 4AMR simulations 66
4.9 Row-averaged pressure profiles extracted from the tube centerline at representative times for the 10PPI 4AMR (blue), 10PPI 3AMR (orange) and Null 3AMR (red) simulations, measured in kPa 69
4.10 Comparison of the development of the leading shock. Pressure ratio (top) and shock components (bottom). Simulations are denoted as 10PPI 4AMR (blue), 10PPI 3AMR (orange) and Null 3AMR (red). 70
4.11 Smear plot of temperature decrease over pores (10PPI 4AMR) 73
4.12 Smear plot of temperature decrease over pores (10PPI 4AMR), porous region denoted in grey. Temperature profile is taken at 65% toward wall to avoid wall noise. Specifically referring to the region denoted in green in Fig. 4.11. 74

4.13 Smear plot of y-velocity profile in region of core temperature drop 75
4.14 Developed pressure field of the Null 3AMR simulation 76
4.15 Pressure perturbations emanating from the pore edges, presented in (a) pressure and (b) y-velocity fields for the 10PPI 4AMR simulation 77
4.16 Comparison of pressure field near wall at t = $\approx 557.5\mu s$, (a) is the 10PPI 4AMR case, (b) is the Null 3AMR case 78

List of Tables

3.1 Summary of simulated cases 40
3.2 AMR level cell sizes 40
3.3 Planar slice positions in centimeters 44

4.1 Normalized integrated differences in bulk flame velocity over 1 cm intervals 56
4.2 Normalized integrated differences in bulk flame velocity over the complete 4–10 cm interval 56
4.3 Distribution of Collected Data 58

Chapter 1

Introduction

Under certain conditions, a subsonic flame can spontaneously accelerate and transition into a detonation, a phenomenon known as deflagration-to-detonation transition (DDT). This transition represents one of the most complex and consequential events in combustion, appearing both as a hazard to be prevented in industrial storage facilities, and as a mechanism to be exploited in next-generation propulsion systems. Understanding and controlling DDT is therefore a problem of both safety and performance.

1.1 Deflagration vs Detonation

There are two forms of combustion, deflagration and detonation, which are divided by the natural speed limit of the transmission of pressure, the local speed of sound [67].

1. Deflagration is a combustion wave that propagates through the unreacted mixture

at a speed lower than the local speed of sound, with propagation governed primarily by heat and species diffusion.

2. Detonation is a combustion wave that propagates through the unreacted mixture at a speed greater than the local speed of sound in the unreacted gas and is coupled to a leading shock wave.

Deflagration is characterized by a reaction front that propagates subsonically relative to the unreacted mixture and is commonly approximated as a near constant pressure combustion process. The reaction is exothermic and the energy produced in the reaction heats and expands the product gases, as the mechanism for the continued onset of the reaction is caused by heat transfer [48]. It becomes self-propagating when the decomposition and volatilization of the reactants produces more energy than it takes to raise the reactants to their ignition temperature [2]. It should be noted that the subsonic nature of deflagration allows pressure waves and perturbations to propagate through and interact with the flame. These interactions can produce combustion instabilities, including thermoacoustic coupling between pressure oscillations and unsteady heat release, which may amplify flame oscillations or contribute to flame quenching [25, 110]

Due to the supersonic nature of detonation, a shock wave is formed that couples to the surface of the flame. Detonation is characterized as a near constant-volume reaction [56, 48]. Decomposition of reactants into constituent volatiles is performed by the shock wave as the shock heats the reactants to their ignition temperature before they are inducted into the reaction zone of the flame [2, 31]. Detonation wave velocities are typically on the order of kilometres per second, although the characteristic velocity depends strongly on

the reactants and their thermodynamic state. Gaseous detonations commonly propagate at approximately 1500 m/s to 3000 m/s [93], while condensed-phase energetic materials can exhibit detonation velocities of several kilometres per second and, for some explosives, approach 10 km/s [100]. For example, stoichiometric ethylene–oxygen, the mixture considered in this study, has a characteristic detonation velocity of approximately 2300 m/s, compared with a laminar flame speed of approximately 5.5 m/s under comparable initial conditions [108, 11, 109].

The detonation wave structure consists of a leading shock wave that compresses and heats the unreacted mixture, followed by an induction zone in which the shocked reactants undergo chemical induction before entering the reaction zone. Within the reaction zone, rapid heat release supports the leading shock as the reactants are converted to products. For an ideal Chapman-Jouguet detonation, the end of the reaction zone corresponds to a sonic plane relative to the propagating detonation front, downstream of which the product gases expand [56].

As the flame is preceded by a shock wave, pressure waves and perturbations are unable to be transmitted through the flame and instead serve only to drive the wave forward. Transverse shock waves generated behind the detonation front interact through reflection and collision, producing localized explosive events within the reaction zone. These microscale interactions provide a mechanism for transferring energy from the chemical reactions behind the shock front to the leading wave structure, effectively driving the detonation wave in a manner analogous to a piston [18]. A detonation wave is therefore a self-propagating structure. Detonation produces less entropy than deflagration, making it capable of achieving higher thermodynamic efficiencies [28].

It should be noted that the preceding definitions describe premixed combustion, in which the reactants are uniformly mixed prior to ignition, as is the case for the work presented in this thesis. In contrast, non-premixed combustion involves separate fuel and oxidizer streams, such that combustion is governed by both chemical kinetics and turbulent mixing. Consequently, local variations in mixture composition and equivalence ratio influence the combustion process and can significantly alter flame behaviour.

1.2 Application of Detonations

Essentially all commercially available engines prior to the end of the 20th century relied on deflagration rather than detonation. This includes gas turbines for power generation and propulsion, as well as internal combustion engines for automobiles, generators, and ships. These engines operate under the Brayton and Otto combustion cycles [116]. These cycles consist of isentropic compression, near constant-pressure heat addition, isentropic expansion, and near constant-pressure heat rejection. Even rocket engines, which operate using an open combustion cycle, rely on deflagrative combustion. Unsteady combustion concepts nevertheless have a long history, with pulse combustion devices investigated throughout the twentieth century and employed in applications including propulsion and heating [82]. Detonation engines, however, present additional challenges associated with controlling detonative combustion and managing the accompanying thermal and structural stresses. The tightly coupled shock-wave and chemical reaction dynamics also occur over very small spatial and temporal scales, making these processes difficult to characterize. Advances in experimental diagnostics, numerical methods, and computational resources have therefore

improved the ability to investigate these processes and develop practical detonation based propulsion systems.

Deflagrative engines have remained dominant because they are highly mature. However, this maturity also means that achieving major efficiency improvements is increasingly difficult. Detonative engines represent a potential 20% improvement in thermodynamic efficiency [113] compared with deflagrative engines. This improvement is primarily associated with pressure-gain combustion, in which the leading shock wave compresses and preconditions the reactants prior to heat release, increasing the pressure of the combustion process and enabling greater work extraction from the expanding products. Although pressure gain has been experimentally demonstrated, the theoretical efficiency improvements associated with detonative combustion have not yet been fully realized in practical engines due to losses introduced by non-ideal operating conditions. These losses arise from the difference between idealized thermodynamic models and the complex requirements of practical propulsion systems, including mixing, heat transfer, and flow losses. Addressing these limitations remains an active area of research in the development of detonative propulsion systems [85].

There are three primary types of detonation engines that have been proposed, the Pulse Detonation Engine (PDE), the Oblique Detonation Engine (ODE), and the Rotating Detonation Engine (RDE). The use of detonative combustion in thermodynamic cycles was first considered by Zel'dovich in 1940 [113]. Jacobs independently developed a thermodynamic treatment of detonation in 1956, which was later elaborated by Fickett and Davis into what is now referred to as the Fickett-Jacobs cycle [28, 40]. The PDE, ODE, and RDE, were all proposed by James Arthur Nicholls between 1957 and 1958 [76].

In the PDE, the propellant is ignited and a detonation wave propagates through the tube, driven by the piston effect generated by the expansion of high-pressure combustion products behind the wave. As the detonation wave reaches the open end of the tube, the expanding products produce thrust through the generation of momentum in the exhaust flow. The subsequent expansion and wave reflections within the chamber assist in exhausting the combustion products, allowing the chamber to be refilled with fresh propellant before the next detonation cycle. This is an intermittent form of thrust, as the chamber must empty the exhaust products that expand behind the detonation wave and then refill with fresh propellant before firing again. Therefore, the engine is often arranged as an array of PDEs that are ignited out of phase such that the vehicle perceives a more continuous thrust. The first test aircraft powered by an array of PDEs was flown out of Wright-Patterson Air Force Base in 2008 [4]. The intermittent operating cycle of the PDE causes significant igniter wear and only approximates continuous thrust.

The ODE, also called a standing detonation wave engine, is an air-breathing detonation engine developed for hypersonic flight as a scramjet system. It is intended to operate at high Mach conditions ranging from Mach 8 to Mach 15. The shape is broken down into a converging inlet, a constant area annular combustor and a de-Laval nozzle [63]. The detonation wave is situated in the combustor at an oblique angle to the direction of the flow of gases. The converging inlet compresses incoming air under ram pressure where it is mixed with the fuel and shock-combusted with a standing detonation wave that is held at an equilibrium position in the combustor. The ignition is shock-induced. Rubins et al. conducted the first experimental wind tunnel tests which were conducted in a Mach 3 tunnel in 1959 [88, 87].

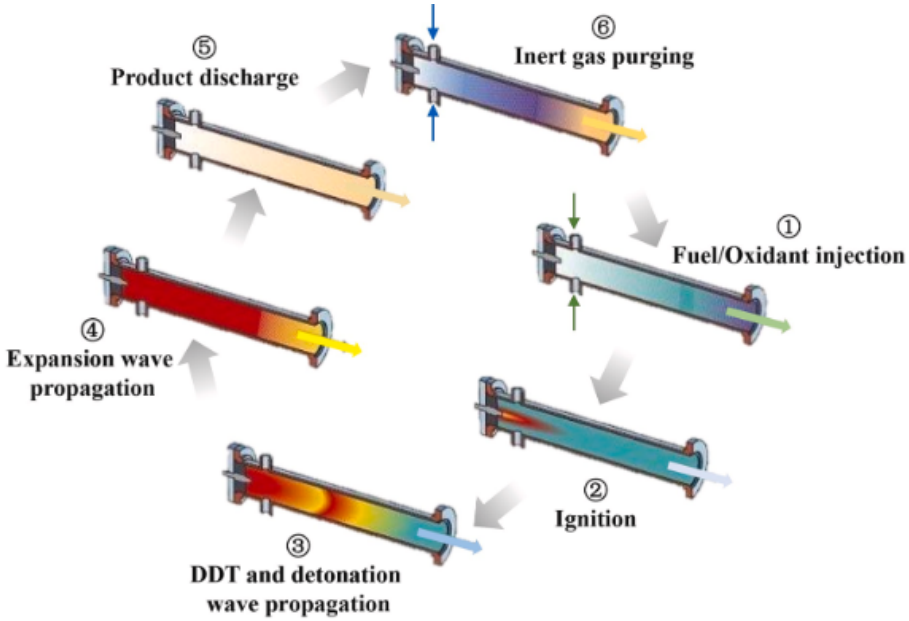

Figure 1.1: Schematic diagram of PDE single cycle. Reprinted from Applied Thermal Engineering, Vol. 244, Y. Li, S. Qi, Q. Jing, L. Zhang, D. Wang, C. Shi, H. Xu, Y. Li, Z. Wu, R. Zhou, The effect of operating frequency and ignition energy on JP-10/PO/aluminum powder multiphase-pulse-detonation-engine, 122758, Copyright (2024), with permission from Elsevier. [59]

While Nicholls proposed the RDE, it was B.V. Voitsekhovskii of the Soviet Union who produced the first experimental prototype in the 1960s using acetylene-oxygen mixtures [83]. An RDE uses an annular ring shaped combustion chamber instead of the conventional cylinder used in deflagrative rocket engines. A detonation wave must be ignited and fed tangentially in the annular chamber while propellants are injected axially, perpendicular to the detonation wave. This results in the detonation wave continuously traveling around the chamber combusting the flow of fresh propellants. The detonation wave is confined between the injector plate and the inner and outer walls of the chamber, allowing an oblique shock wave to break free only in the axial direction. The oblique shock wave redirects gases out of

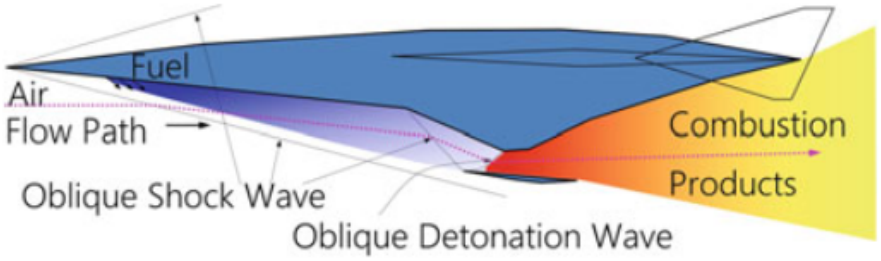

Figure 1.2: Schematic diagram of Standing Wave Detonation Engine. Reprinted from Proceedings of the Combustion Institute, Vol. 34, P. Wolański, Detonative propulsion, 125–158, Copyright (2013), with permission from Elsevier. [107]

the chamber to produce thrust. The wave travels at speeds on the order of kilometres per second, meaning that the detonation wave traverses the length of the chamber thousands of times per second. As a result, the exit plane experiences quasi-continuous thrust. The advantage is that it requires only one ignition and has fewer parts which reduces mass. The disadvantage is that it has more wall area that requires a solution for thermal management. The first operation of an RDE outside of lab testing was conducted by the Japan Aerospace Exploration Agency (JAXA) in which an RDE was test-fired in space aboard the sounding rocket S-520-31 in 2021 [1]. Later in 2025, the world's first RDE-powered rocket was launched by Venus Aerospace [103]. Recent developments have also demonstrated the potential integration of RDE combustion with turbo-machinery for power generation. In 2026, researchers at Karlsruhe Institute of Technology (KIT) demonstrated a hydrogen fueled compressor-less gas turbine using pressure-gain combustion, achieving a continuous operating duration of 303 seconds and successfully generating electricity through a coupled turbine [47].

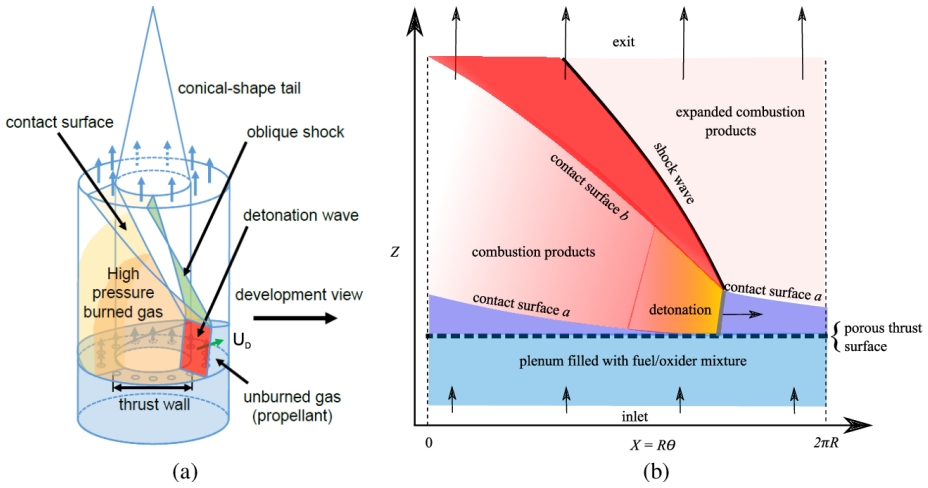

Figure 1.3: Schematic diagram of Rotating Detonation Engine. Reproduced from Shepherd and Kasahara, 2017 [94]

1.3 Initiation of Detonation

A key challenge for all of these engines is achieving repeatable and stable ignition followed by the formation of detonation. Detonations form in two ways, the direct initiation of a detonation in a reactive medium, or the transition of a deflagrative (often called slow moving) flame into a detonation as it propagates through a reactive medium[53].

The direct initiation of a detonation is difficult to achieve in a gaseous mixture due to the low energy density of the reactants compared to liquid or solid reactive media. Additionally, the gases can be compressed which gives freedom for the particles to be pushed away in response to pressure during an ignition event, instead of initiating a reaction. The magnitude of the initial energy release is a significant variable in achieving direct initiation[53]. If the energy deposition doesn't occur over a fast enough time and into a small enough volume then the resulting blast will decelerate below the Chapman-Jouget

(CJ) velocity of the mixture and decay into an acoustic wave [26]. The required energy, known as the critical energy for initiation, is three to four orders of magnitude higher than the minimum ignition energy required for a slow moving deflagrative flame, depending on the initial conditions [115, 42]. ODEs are able to achieve the conditions necessary for direct initiation, but they require the inlet air to be traveling on the order of Mach 5 to do so.

Due to the challenge of direct initiation in gaseous reactants, an alternative method of initiating a detonation is to accelerate a deflagrative flame through deflagration-to-detonation transition (DDT). An RDE can be ignited by first initiating a flame within a DDT tube and, after the onset of detonation, directing the resulting detonation wave tangentially into the Rotating Detonation Chamber (RDC). In the case of PDEs, DDT can instead form part of the operating cycle: a deflagrative flame is initiated in a relatively quiescent reactive mixture and accelerated until transition to detonation occurs before the wave exits the tube and produces the thrust pulse.

Starting with an established plug flame that is anchored to the chamber walls, *Figure* 1.4, the process of DDT is such that[71]:

1. The flame releases energy into the surroundings, causing pressure perturbations ahead of the wave and an increase in turbulence

2. The turbulence causes wrinkling of the flame surface which increases the local surface area of the flame

3. The increased flame surface area increases the rate of reaction which releases more energy into the surrounding mixture and increases the intensity of the leading pressure

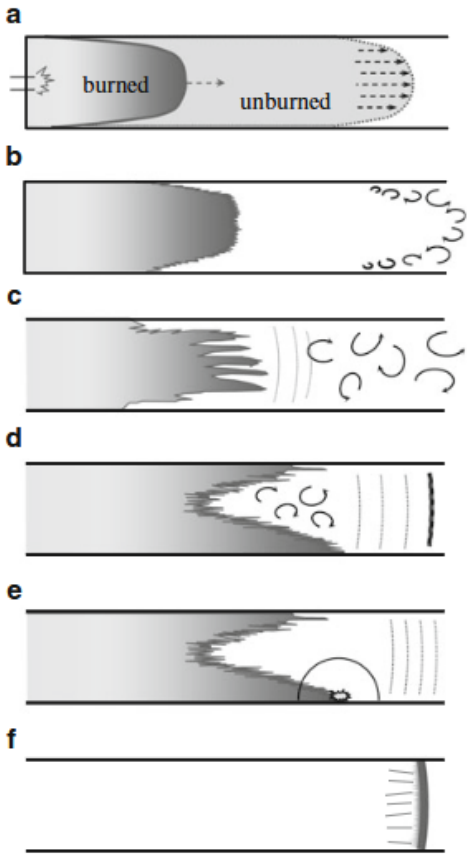

Figure 1.4: Schema of a gas DDT in a closed tube. Reproduced with permission from McAfee, J. M., "The Deflagration-to-Detonation Transition", Shock Wave Science and Technology Reference Library, Vol. 5: Non-Shock Initiation of Explosives, 2010, Springer Berlin Heidelberg. © 2010 Springer Nature [71]

perturbations

4. The increased energy release causes more turbulence, which increases the intensity of the wrinkles in the flame surface until the flame develops local twists, increasing the effective flame surface area and accelerating the overall flame propagation

As this positive feedback process continues, the increasing flame-surface distortion

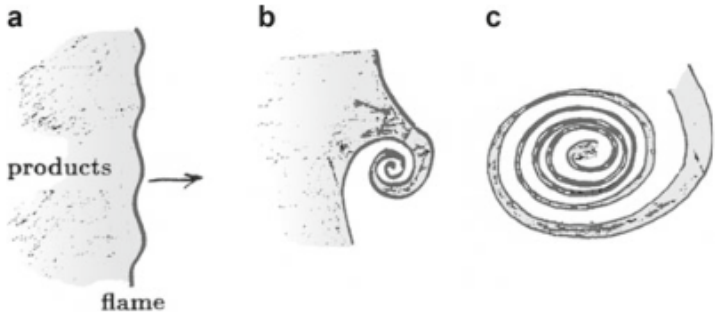

Figure 1.5: Schema of vortical amplification. Reproduced with permission from McAfee, J. M., "The Deflagration-to-Detonation Transition", Shock Wave Science and Technology Reference Library, Vol. 5: Non-Shock Initiation of Explosives, 2010, Springer Berlin Heidelberg. © 2010 Springer Nature [71]

can develop into high-pressure vortical structures called jelly rolls, *Figure* **??** *c*, containing mixed and sandwiched layers of $reactants \rightarrow flame\ surface \rightarrow products \rightarrow flame\ surface \rightarrow reactants$ [53, 56, 71, 95]. The leading pressure perturbations coalesce into a leading shock wave ahead of the accelerating flame. As the flame accelerates and approaches the shock, compression of the unreacted mixture between the two structures increases the local temperature and pressure, producing conditions that can initiate localized explosive events between the flame and shock [50]. These explosive events accelerate the flame front, promoting coupling between the reaction zone and the leading shock wave to form a shock-flame structure with supersonic propagation velocity. This structure alone represents an overdriven, also called an "overcharged," deflagration wave. Detonation is achieved when the production of turbulence supports the formation of transverse shock waves behind the primary coupled shock-flame structure [93]. The interactions of these transverse shock waves provide the mechanism required for self-sustained propagation of the detonation wave.

These phenomena represent an energy transfer occurring at a microscale. The macroscale detonation wave structure is made up of microscale detonation cells. These cells are separated by triple points where the transverse shock waves meet the leading shock wave and subdivide it. Each cell represents a micro detonation that is a part of the macro wave [29].

When a microscale detonation is initiated, it begins with a velocity significantly greater than the Chapman-Jouguet velocity, reaching approximately $1.6U_{CJ}$[54]. As the detonation structure expands, its velocity decreases as energy is redistributed through the surrounding wave system, eventually entering a decaying phase. The evolution from initiation to decay can be considered the lifecycle of a microscale detonation cell. Adjacent microscale detonation cells exist simultaneously at different stages of this life cycle, with the boundaries of each cell defined by the transverse shock waves associated with triple-point motion. A diagram of the regions within the detonation wave structure is shown in Figure 1.6, and the corresponding detonation cell traced by the motion of the detonation wave is shown in Figure 1.7.

As neighbouring detonation structures interact, the transverse shock waves converge and generate localized regions of high temperature and pressure capable of initiating a new microscale detonation. The newly initiated detonation begins a growth phase while the neighbouring structures enter a decay phase. As these older structures weaken, the expanding detonation structure occupies the region previously dominated by the decaying cells. This process repeats continuously, with the interactions between transverse shock waves providing the mechanism for transferring energy from chemical reactions occurring behind the shock front into the forward propagation of the macroscale detonation structure. The transverse shock waves therefore enable self-sustained propagation by con-

tinuously generating new microscale localized explosive events to replace those undergoing decay within the macroscale detonation structure. It should be noted that the "cells" are not three-dimensional bubbles as might be inferred from the terminology. Instead, they represent the path traced by the motion of the subdivided detonation plane over time [29, 56, 106].

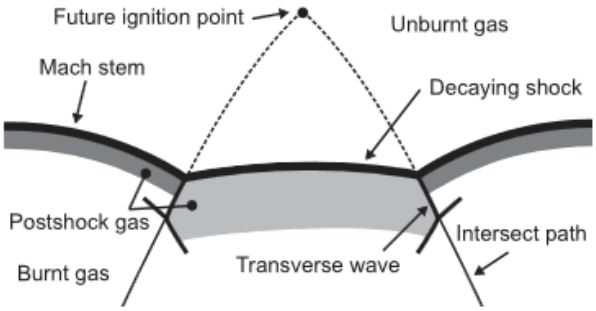

Figure 1.6: Schematic of Detonation Wave Structure. Reprinted from Proceedings of the Combustion Institute, Vol. 38, J. Crane, X. Shi, J. T. Lipkowicz, A. M. Kempf, H. Wang, Geometric modeling and analysis of detonation cellular stability, 3585–3593, Copyright (2021), with permission from Elsevier. [19]

The preceding discussion describes the physical processes governing the transition from deflagration to detonation. These processes can be summarized into the following criteria, all of which must be satisfied for a self-sustaining detonation to be established:

1. Reactant concentration must be above the detonability limits of the mixture
2. The ignited flame must be accelerated beyond the CJ deflagration velocity of the mixture
3. A shock wave must form and couple to the flame in a shock-flame structure

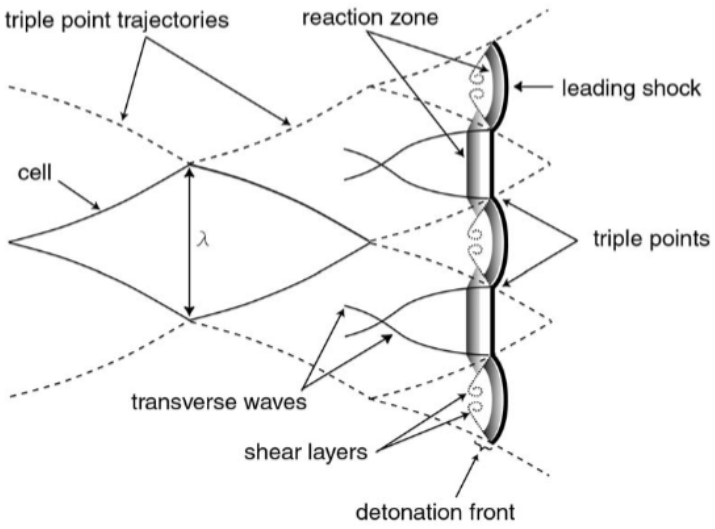

Figure 1.7: Detonation Wave Cellular Structure. From "Experiments in gasdynamics of explosions," by A. K. Oppenheim and R. I. Soloukhin, 1973, Annual Review of Fluid Mechanics, 5, Copyright 1973 by Annual Reviews. Reprinted with permission. [77]

4. Hot spots and a rapidly compressing pressure gradient needs to form between the flame and the leading shock such that a spontaneous detonation is initiated

5. Transverse shock waves must be present to cause the direct initiation of micro-detonations such that the structure is self-propagating through the reactive mixture

DDT can occur naturally when a deflagrative flame is confined to a tubular domain that is filled with a reactive mixture. The natural process of DDT takes place over a run-up distance that is significantly larger than the diameter of the confining tube. Mejia-Botero assembled a database of unobstructed DDT experiments [72]. This database indicates that the DDT run-up distance can be a factor of $10 - 250$ times larger than the diameter of the confining tube. As the process of operating a PDE is itself the process of DDT, and RDEs are ignited from DDT, the study of the transition is of clear interest to modern propulsion

engineers who want the DDT process to be greatly shortened. This is balanced from a safety perspective because the onset of DDT can occur in pipelines of gaseous or vaporous reactants such as hydrogen and steam. In these cases a long run-up distance is desirable to prevent the conversion of a weak flame into a detonation. For these reasons, DDT has been studied with both the goal of accelerating and suppressing the process.

Porous structures have a history of extensive investigation for the attenuation of flames and pressure waves in industrial applications. Their ability to increase heat transfer, provide large surface areas for thermal losses, and disrupt propagating pressure disturbances has led to their use in flame arresters and other explosion protection systems [27, 6, 8]. However, the influence of a porous medium is strongly dependent on its geometry, material properties, cell state open vs closed cell, and interaction with the reacting flow. Under some conditions porous structures can attenuate or extinguish flame propagation, while under others they can promote flame acceleration and facilitate the onset of detonation [41, 62].

Porous structures have recently been investigated as a means of influencing combustion and detonation behaviour in propulsion systems. In rotating detonation engines, porous structures have been proposed as potential injector interface materials as a means of managing propellant mixing, and influence interactions between the detonation wave and injection system. Experimental investigations by Jiang [41] and Lin [62] demonstrated that porous copper structures can significantly influence flame acceleration and detonation initiation during DDT. Their observations indicated that combustion within the porous structure contributed to bulk flame acceleration. Motivated by the significance of understanding DDT, the objective of the present work is to investigate the influence of a porous

boundary condition on flame acceleration, pressure field development, and shock formation during deflagration-to-detonation transition through high-fidelity numerical simulation. By comparing a smooth-wall configuration with a porous-wall configuration representative of the experiments of Jiang and Lin, this study seeks to improve the understanding of the physical mechanisms through which porous structures influence flame propagation and the development of the leading shock.

The remainder of this thesis is organized as follows. Chapter 2 presents a review of the literature relevant to DDT, including the historical development of DDT mechanisms and experimental and numerical methods used to promote transition. Chapter 3 describes the numerical methodology, governing equations, computational domain, boundary conditions, and simulation setup employed in this study. Chapter 4 presents the simulation results and the evolution of the flow field as it interacts with the defined porous boundary conditions. Chapter 5 discusses the results in the context of existing DDT theory and experimental observations. Finally, Chapter 6 summarizes the principal findings of this work.

Chapter 2

Literature Review

The aim of this literature review is to study the historical context of the progression of DDT research and the methods used by those advancing this field such that this thesis can be understood for its contribution to the greater body of work. The review is broken down into sections for the historical progression of the development of DDT mechanisms, experimental and numerical methodologies, and finally the motivation of this study.

2.1 Historical Development of DDT Mechanisms

In 1883 Ernest Mallard and Henri Le Châtelier produced their foundational model of laminar flame propagation [66]. That a flame preheats unburnt gases around it until the surrounding regions of gas reach their auto-ignition temperature and the flame spreads. In the experiments of this work they used a rotating drum camera and were the first to observe the transition from deflagration to detonation [56]. This demonstrated the

possibility of two modes of combustion existing in the same gaseous mixture. Mallard and Le Châtelier then suggested that the chemical reactions in a detonation wave are initiated by the adiabatic compression of the detonation front.

The observations recorded by Mallard and Le Châtelier confirmed a transition between deflagration and detonation, but criteria for achieving the transition, and even for defining what a detonation was were necessary. The thermodynamic foundation for shock waves in reacting gases was established through the conservation relations derived by Rankine and Hugoniot in 1887 [86, 38], which relates thermodynamic states across a discontinuity via the Rankine-Hugoniot jump conditions and the associated Hugoniot curve. Building on the works of Rankine and Hugoniot, both David Chapman (1899) and Émile Jouguet (1905) contributed to defining criteria for selecting a solution out of a family of possible end states behind a shock [13, 45]. In modern physics this is known as selecting from the strong and weak solutions across a deflagration and detonation wave, but this wasn't formalized until reactive-flow theory in the 1970s. Chapman calculated the velocity of an explosion in a gaseous explosive mixture (GEM) and identified a minimum propagation speed for a self-sustaining detonation, a minimum velocity for the minimum detonation solution. Jouguet investigated the locus of thermodynamic states for various detonation velocities and proposed that the minimum detonation solution corresponded to the solution with the minimum entropy. Both independently noted that their respective solution occurred when the conditions downstream of the detonations were at sonic conditions. It was Louis Crussard in 1907 [20] who formally acknowledged this, resulting in the minimum detonation criteria, or sonic conditions, becoming known as the Chapman-Jouguet (CJ) criteria. It should be noted that Vladimir Mikelson (1890) independently developed a similar theory

of gas dynamic detonations, but his findings were published exclusively in Russian with limited dissemination outside of Russian literature, so credit is attributed to Chapman and Jouguet [56].

Following the establishment of detonation theory, attention turned toward the experimental control and augmentation of DDT which is spoken of in Section 2.2 Experimental Investigation of DDT. Progress in the mechanisms of DDT wasn't enabled until advancements in high-speed flow visualization was achieved during the 1950s and 1960s. Particularly, the development of self-synchronizing stroboscopic schlieren techniques capable of resolving rapidly evolving shock and combustion structures by exposing changing density fields in a gaseous mixture [91, 102]. These diagnostic methods allowed Oppenheim and his collaborators to directly observe the wave interactions accompanying DDT, revealing phenomena that had previously been inferred only from pressure measurements and post-test observations. Subsequent investigations by Oppenheim and Urtiew employed stroboscopic schlieren photography and lead to the observation of localized explosive events embedded within the accelerating flame front. This was referred to as the "explosion within an explosion" concept [102, 50].

A theoretical explanation for the localized ignition events was later proposed by Zel'dovich in 1970. Zel'dovich demonstrated that a sufficiently shallow induction-time gradient, primarily governed by temperature, could produce a spontaneous reaction wave. Since ignition occurs first in the hottest region, the resulting reaction front propagates through the gradient and, under suitable conditions, may couple with a shock wave to form a detonation [114]. Building upon both the experimental observations of Oppenheim and Urtiew and the theoretical framework of Zel'dovich, Lee (1977) described DDT as a coupled process

involving turbulence, flame acceleration, vortex formation, and shock amplification. In this interpretation, turbulent flame structures created localized regions of elevated temperature and pressure where rapid energy release may occur, providing a physical pathway for the direct initiation events observed experimentally and the subsequent formation of a self-sustaining detonation [53].

These concepts were subsequently formalized through the Shock Wave Amplification by Coherent Energy Release (SWACER) mechanism. In the SWACER framework, localized energy release occurring behind a shock wave strengthens the shock, which in turn promotes additional reaction and further energy release. This positive feedback process provides a mechanism by which localized ignition events can evolve into a self-sustaining detonation and serves as a unifying description connecting the experimental observations of Oppenheim and Urtiew with the induction-time gradient theory proposed by Zel'dovich and the turbulence-driven initiation process described by Lee [56].

2.2 Experimental Investigation of DDT

After the establishment of detonation theory, work began on attempting to understand how the process of DDT can be affected and controlled by augmenting its confinement. Early experimental investigations into the influence of confinement geometry on detonation formation can be traced to the work of Paul Laffitte in the early 1920s. In his studies of explosive-wave propagation, Laffitte introduced wall roughness by lining the interior of a tube with coarse sandpaper and observed that surface irregularities significantly influenced the formation and propagation of explosive waves [51, 52, 56]. Surface roughness

turned into obstacles in the works of Wheeler and Chapman (1926) who took the experimental apparatus used by Mason (1923), a brass combustion tube open at both ends, and systematically inserted restricting rings to the inside of the tube [14]. Chapman and Wheeler demonstrated that an otherwise laminar methane-air flame traveling at 14 cm/s in a smooth tube could be accelerated to 420 m/s by placing the restricting rings with a blockage ratio of 0.5 into the path of the flame. They observed retardation of the flame leading up to the obstacle and acceleration afterward. When multiple obstacles were inserted and spaced close together, only the acceleration was observed in the subsequent obstacles.

Shchelkin (1940) further demonstrated the impact of obstacles as a means of artificial surface roughness [92]. Motivated by industrial and mining explosions, Shchelkin's work was conducted in the context of safety research, where understanding the influence of confinement and wall roughness on flame acceleration and detonation formation was of practical importance. He produced artificial roughness in a tubular gaseous combustion chamber by lining the inner wall with a helical spiral, later known as a Shchelkin Spiral. He observed that adding the spiral or rough structure obstacles causes much faster flame propagation, stronger pressure buildup ahead of the flame, and earlier shock formation. The distance required for DDT becomes much shorter in rough tubes and detonation becomes easier to sustain once formed even though the detonation velocity is reduced relative to the CJ velocity. This produced the idea of extending the limits of detonability through wall and obstacle interactions.

Shchelkin demonstrated that roughness dramatically reduced the predetonation distance from $20 - 40$ tube diameters, down to the order of $2 - 4$. Babkin and Kazachenko

(1960) subsequently employed high-speed schlieren photography to investigate the underlying mechanism and observed the formation of a coupled shock-flame structure, where the flame and the shock were moving at the same sub-detonation velocity as the shock strengthened. They proposed that reflections of the accelerating shock from roughness elements continuously ignited mixture near the tube walls, changing the ignition mechanism from purely turbulent flame propagation to a shock-assisted process that ultimately evolved into detonation [3].

While Babkin and Kazachenko continued the roughwall experimentation of Shchelkin in Russia, in America Evans (1955) was examining lining the combustion tube wall with acoustically attenuating materials [27] as it had been shown a priori that as a planar wave travels over attenuating materials, energy is lost from the wave to the absorbing medium [89]. Evans used a porous sintered bronze lining and reported that it increased the run-up distance for DDT by attenuating the pre-compression waves ahead of the accelerating flame.

Wagner revisited the work of Chapman and Wheeler by systematically investigating flame interaction with single and multiple orifice plate obstacles. Advancements in instrumentation enabled pressure measurements upstream and downstream of each obstacle, along with high-speed photography of the flame propagation. He demonstrated that flame acceleration doesn't depend on the shape of the orifice it is passing through, as long as the blockage area remains the same. An optimum orifice-to-tube area ratio for pressure generation was identified. Additionally, it was shown that sequential obstacles produce cumulative pressure amplification that culminated in shock-like pressure profiles after sufficient run-up distance [104]. This work was also continued by Lee in 1984 who utilized

both orifice plates and the Shchelkin Spiral. Lee found that increasing blockage ratio increased the pressure losses across the obstacles and simultaneously enhanced flame acceleration. He attributed this behaviour to the conversion of flow energy into turbulence, which increased the combustion rate and promoted flame acceleration [57]. Lee further noted, consistent with the earlier observations of Oppenheim and Urtiew [102], that the abrupt transition to a quasi-detonation regime is associated with a minimum critical flame speed. Peraldi later confirmed this criterion in 1988, demonstrating that the critical flame velocity corresponds approximately to the local speed of sound in the unburned mixture ahead of the flame [79]. It was additionally observed that a lower limit exists for blockage ratio. The characteristic opening dimension must remain sufficiently large relative to the detonation cell size, specifically it must permit the passage of at least one detonation cell, otherwise the developing detonation may be quenched as it attempts to propagate through the obstacle field.

The study of obstacle-induced flame acceleration continued into the late 2000s with the work of Ciccarelli and Johansen, who investigated flame propagation in channels containing repeated wall-mounted obstacle arrays. This work built upon earlier investigations by Lee [55], Chue [15], and Gamezo [30], which identified multiple regimes of flame acceleration and highlighted the growing importance of shock-flame interactions as the transition progressed. Ciccarelli and Johansen demonstrated that the early stages of flame acceleration are dominated by turbulence-induced increases in flame surface area, whereas the later stages are governed by shock-flame interactions and repeated interactions with shocks reflected from the obstacle surfaces [44, 17]. Fence-type obstacles were revisited by Liu in 2022 with a focus on obstacle geometry. Rectangular and triangular configurations were

examined, with triangular obstacles producing shorter DDT run-up distances at lower blockage ratios. The inclined surfaces promoted stronger flame-vortex interactions and improved the survivability of localized secondary explosions, thereby facilitating completion of the DDT process [64]. These observations are consistent with the earlier findings of Ciccarelli, who showed that reflected shocks generated by the obstacles grow in strength during the later stages of acceleration and can become sufficiently intense to alter the flame's interaction with the obstacles themselves [17].

The control of detonation is of interest both for promoting detonation formation in advanced propulsion systems and for suppressing accidental detonation in industrial gas applications. The dual role of porous media in both promoting and suppressing combustion can be traced to the interaction between reacting flows and solid surfaces. Zel'dovich proposed in 1941 a one dimensional theory of flame quenching, that when the diameter of a passage is comparable to the thickness of the flame, the heat loss into the walls of the passage is sufficient as to quench the flame as the energy produced is lost to the walls instead of to promoting flame propagation [112]. Indeed this was observed by Gou in 2002 who lined the walls with steel wool and found it to be more effective at attenuation than perforated plates due to the high surface area [33]. This is what makes porous media attractive for flame and detonation suppression as the media is filled with tortuous passages and significantly increased wall surface area for heat loss. Porous media re-emerged as a subject of DDT research in the work of Ciccarelli and Johansen in 2008 by studying a horizontal tube half filled with ceramic beads and compared it to the same tube with dimpled surfaces comparable to the bead shape. It was found that the flame propagation in the bead layer drove flame acceleration in the gap as the flame propagated faster in the

beads and ignited the mixture above. While DDT did not occur in the packed bed of beads as the pore size was too small for self sustained detonation, a non self sustaining explosion front was observed propagating through the bead layer. It was concluded this was due to the formation of strong shocks in the bead layer compares with weak compression waves propagating in the gap. The strong shocks auto-ignite the mixture in the bead layer [43]. Ultimately, this resulted in a DDT run-up distance of only ten tube diameters. In contrast to rigid packed-bed structures, Bivol, Golovastov, and Golub, in the late 2010s, observed that compliant porous coatings such as polyurethane foam reduced detonation velocity and promoted wave attenuation. The open-cell elastic structure deforms under shock loading, dissipating energy and disrupting the formation of transverse shock structures that are necessary for sustaining a detonation [6, 8]. These observations demonstrate the dual role of porous media in either promoting or suppressing DDT, depending on the pore geometry, material properties, and resulting flow interactions.

The combined body of work on porous and highly subdivided structures demonstrates that distributed media can significantly alter both flame acceleration and detonation propagation through a competition between heat loss, turbulence generation and shock formation. Early concepts of porous wall attenuation originating from Evans evolved into studies of rigid packed beds, where strong confinement and tortuous pathways promote distributed ignition and localized shock formation. In contrast, more compliant porous coatings and foams have been shown to attenuate detonation waves through enhanced energy dissipation and disruption of coherent shock structures. The results collectively highlight the duality of porous media for designing systems when regarding DDT. Recent work, motivated by PDE application, has focused on designing porous wall configurations that exploit the

flame acceleration benefits of distributed media. Work by the research group of Jiang et al in 2024 and later reported on by Lin et al in 2025 studied DDT in a square tube that had rigid copper foam lining the top and bottom of the tube. Systematically studying the impact of pore size from 10 pores per inch (PPI) to 50 PPI it was observed that larger pores significantly shortened the run-up distance of DDT down to a reported six tube diameters [41, 62]. Attenuation of the detonation was experienced at a 3% CJ velocity deficit. Collectively, these results conclude the experimental progression from discrete obstacle fields toward distributed porous structures for controlling DDT behaviour.

2.3 Numerical Approaches for DDT Simulation

In parallel with experimental investigations, theoretical and numerical modelling of DDT has developed as a complementary approach for examining reactive compressible flow phenomena that are difficult to isolate experimentally. Merzhanov and Borisov analytically modeled hot spots capable of DDT ignition [73, 9] while Zajac, Meyer, and Oppenheim modeled the flame as an expanding piston [111, 74]. As this coincided with the emergence of Zel'dovich's compression field analysis, it rode along the experimental perspective as a way of modelling DDT as computational modelling of compressive reactive flows was still a significant distance away. In 1984 the first modelling of a flame-shock interaction was conducted by Picone in which the flame was simplified into a hot expanding bubble that separated unburned gas from cold background gas by a non-reacting, discontinuous interface [80]. As computational resources improved, reactive flow simulations began incorporating increasingly realistic chemistry and flow physics. Oran and Gamezo as late as

the 1990s began their initiative with the Naval Research Laboratory to comprehensively simulate DDT. Oran wrote even then that while a 2D simulation may take weeks to run, a 3D simulation would take 1000 years. Their project culminated in a major synthesis of their work in 2006, demonstrating through multidimensional reactive Navier-Stokes simulations that hydrodynamic instabilities, shock-flame interactions, and localized energy release could be resolved numerically and linked directly to experimentally observed DDT behaviour [78].

More recent numerical studies have applied these capabilities to increasingly small-scale and highly resolved configurations. Han et al. [34] numerically investigated ethylene-oxygen flame acceleration and DDT in a microchannel, observing substantial axial flame stretching during flame acceleration. Ramachandran et al. [84] similarly investigated hydrogen flame propagation in a micro-channel and observed the development of flame wrinkling and finger-like structures during flame acceleration. Although these viscous-dominated micro-channel configurations differ substantially from larger-scale DDT channels, they demonstrate the ability of modern numerical approaches to resolve the evolving flame structures associated with confined flame acceleration.

Despite substantial advances in available computational resources, numerical simulation of DDT remains challenging because of the wide range of spatial scales that must be represented. In addition to resolving the overall domain, sufficient spatial resolution is required to capture relevant turbulent structures, the flame thickness or induction zone, and shock–flame interactions. Karanam et al. illustrate this challenge using the example of a 1 m domain containing a 0.5 mm flame thickness, for which resolving the flame with (10) computational cells would require on the order of 10^{12} cells in a three-dimensional uniform

grid [46]. Reducing the physical domain does not necessarily eliminate these resolution requirements. In micro-channel simulations, for example, viscous effects and wall heat transfer can become increasingly influential, requiring sufficient resolution of near-wall flow and thermal gradients [108].

The treatment of turbulence introduces an additional challenge because the highly compressible, reacting, shock-driven flow present during DDT differs substantially from the conditions underlying conventional turbulence models [65]. Consequently, both turbulence-resolving and turbulence-modelling approaches have been investigated for detonative flows. Large-eddy simulation (LES) resolves larger turbulent structures while modelling the effects of unresolved subgrid scales and has been applied to simulations of unsteady detonation propagation and cellular structure [21]. Specialized approaches have also been developed for detonative flows, including the Compressible Linear Eddy Model coupled with LES (CLEM-LES), which incorporates subgrid-scale scalar mixing under highly compressible conditions [69, 68]. More recently, reduced-cost turbulence closures such as the one-equation Wray-Agarwal model have also been assessed for detonative reacting flows [90].

Turbulence models provide a means of reducing the computational resources required for simulation by modelling the influence of flow structures that are not directly resolved. However, these approaches necessarily introduce assumptions regarding the behaviour and influence of the unresolved scales. Direct numerical simulation (DNS), in contrast, avoids the introduction of a turbulence closure by directly resolving the dynamically relevant turbulent scales. This substantially increases the spatial and temporal resolution requirements and, consequently, the computational cost of the simulation. The choice between directly

resolving turbulent structures and introducing turbulence models therefore represents a trade-off between computational cost and the assumptions introduced in representing unresolved flow behaviour.

The computational cost associated with resolving the range of spatial scales present in reactive flows can be reduced through adaptive mesh refinement (AMR). Rather than maintaining the finest spatial resolution throughout the entire computational domain, AMR dynamically concentrates computational resources in regions containing flow features requiring greater resolution. Stock and Moureau describe the application of AMR to reactive flows for resolving features including turbulence, shock waves, and flame fronts while reducing the overall computational cost [98]. The effectiveness of AMR consequently depends on the criteria used to identify regions requiring refinement. Feature-based approaches commonly use gradients in flow variables to identify structures such as shocks, vortexes, and combustion fronts.

Numerical modelling of DDT must also consider the choice of chemical kinetic mechanism. Approaches range from one-step Arrhenius mechanisms [35, 37], through reduced chemical mechanisms, to detailed chemical kinetics [37]. Increasing chemical fidelity introduces substantial computational cost due to the increasing number of transported species and the integration of stiff chemical source terms. Simplified global mechanisms reduce this cost by representing combustion through a limited number of global reactions, while reduced mechanisms retain a subset of species and reaction pathways selected to reproduce important kinetic behaviour over a specified range of conditions. Detailed mechanisms provide a more complete representation of processes such as chain branching and radical formation, but at substantially greater computational expense.

Modern numerical investigations of DDT therefore require a balance between physical fidelity and computation feasibility. Spatial resolution, treatment of turbulence, mesh refinement, and chemical kinetics are interdependent choices that determine both the physical processes represented by a simulation and it computational requirements. Advances in high-performance computing, adaptive mesh refinement, and chemical mechanism reduction have enabled increasingly detailed simulations while managing these costs. Numerical modelling consequently provides a means of examining the transient shock-flame, turbulence, and chemical interactions involved in DDT that may be difficult to isolate experimentally, provided that the assumptions and resolution requirements associated with the selected numerical approach are appropriately considered.

2.4 Motivation

The motivation for this work originated from the development of novel injector concepts for rotating detonation engines. Unlike conventional rocket injectors operating under approximately steady chamber conditions, RDE injectors are exposed to the highly transient pressure field generated by the periodic passage of the rotating detonation wave. Immediately following wave passage, the elevated chamber pressure can temporarily suppress injection and drive combustion products upstream into the injector, after which these products must be purged before fresh propellant injection can resume [5, 32]. Goto et al. characterized this behaviour through an effective injector area, representing the fraction of the nominal injector area available to supply fresh propellant following backflow purging. Their results demonstrated that the effective injector area decreases as the ratio of com-

bustor pressure to upstream plenum pressure increased [32]. Consequently, injector design must simultaneously limit backflow and provide sufficiently rapid propellant replenishment to establish the required fresh-mixture layer ahead of the returning detonation wave.

Initial injector concepts considered coupling neighbouring injectors such that energy from detonation-induced reverse flow could be redirected to assist in clearing backflow from adjacent injectors. This concept subsequently evolved toward the use of a porous injection interface. It was hypothesized that the interconnected pore structure could distribute the pressure disturbance associated with backflow across numerous flow passages, thereby limiting the penetration depth experienced by individual injectors. The small characteristic pore dimensions were also expected to provide resistance to flame and detonation propagation into the injection system, while distributed injection through the porous surface offered the potential for improved propellant mixing within the thin RDE chamber. Porous injection has previously been investigated for conventional rocket engines [22], and have recently been proposed specifically for RDEs, where pore dimensions were selected in part according to flame and detonation quenching criteria [49]. However, placing a porous structure in direct contact with the combustion chamber necessitates an understanding of the interaction between the porous surface, flame, and detonation-induced pressure field. The experimental investigations of Jiang and Lin [41, 62] were therefore selected as the basis for studying these interactions and developing an understanding of porous-media modelling relevant to future injector concepts.

At the outset of the project, it was hypothesized that the flame stretching at the pore openings and repeated shock reflections from the pore surfaces would be sufficient to promote deflagration-to-detonation transition, such that the surface interactions of the porous

structure could be isolated as the dominant mechanisms promoting DDT. As the present study progressed, a more comprehensive review of the historical DDT literature revealed that porous media influence detonation formation through a broader range of mechanisms than initial considered. In particular, the works of Ciccarelli and Johansen [43] and Jiang and Lin [41, 62] demonstrated that combustion occurring within the porous body plays an important role in flame acceleration and the promotion of DDT. The present simulations therefore isolate a narrower subset of the physical mechanisms associated with a porous structure: the interaction of the flame and developing pressure field with the exposed porous surface, while excluding combustion within the porous volume. In this representation, the pore openings provide distributed geometric surface disturbances while permitting mass flow out of the computational domain. This distinction allows the influence of the porous surface itself to be examined independently of internal porous combustion, while retaining relevance to the development of porous interfaces for future RDE injector concepts.

Chapter 3

Methodology

Herein, the applied scientific methods are discussed. This includes sections for the software that was used, the governing equations that were numerically solved, the computational domain, discretizations, boundary conditions, and the post-processing methods. The numerical simulation setup is an attempt to reproduce the experimental configurations investigated by Jiang and Lin [41, 62].

The simulations model the propagation of a premixed ethylene-oxygen flame through a rectangular channel, with porous boundaries introduced downstream of an initial smooth-wall region. Simulations were run with pore densities of 0 pores per inch (PPI) which is the null pore condition, and 10 PPI in the porous regions of the domain, to be discussed in Section 3.3 Computational Domain and Geometry. Multiple levels of Adaptive Mesh Refinement (AMR) were utilized as well to improve the allocation of computational resources, this is discussed in Section 3.4 Mesh, Boundary and Initial Conditions. It should

be noted that simulations at 40 PPI were attempted, but the number of pores produced at 40 PPI increased by a factor of 18 which became so computationally costly to initialize that the simulation would not progress into time stepping and solving. Therefore it was opted to remain with 10PPI simulations.

The simulations were run on the Trillium High Performance Computing (HPC) cluster at the University of Toronto and operated by the SciNet High Performance Computing Consortium and the Digital Research Alliance of Canada [23].

3.1 Numerical Framework

Numerical simulations were performed using PeleC [97]. PeleC is a compressible reacting-flow solver that was developed by the AMREX-Combustion team and is supported by the United States Department of Energy's Exascale Computing Project. PeleC solves the compressible Navier-Stokes equations with multispecies transport and finite-rate chemistry and is designed for large scale simulations on high performance computing systems. PeleC employs a Piecewise Parabolic Method (PPM) for higher-order spatial reconstruction in conjuction with a Godunov method and approximate Riemann solvers at cell interfaces. These shock capturing methods allow sharp gradients and discontinuities to be resolves while limiting non-physical numerical oscillations, making PeleC well suited for simulations involving shock-flame interactions, DDT, and detonations.

PeleC uses a second-order explicit method-of-lines (MOL) for time-stepping in conjunction with explicit Runge-Kutta integration. The previously described Godunov method

and approximate Riemann solvers are applied in the computation of the convective fluxes at cell interfaces. Diffusive fluxes, including viscous, thermal, and species diffusion, are evaluated using centered finite-difference schemes. The stiff chemistry source terms are integrated using the C-language Variable-coefficient ODE solver (CVODE). PeleC utilizes a block-structured meshing system with AMR to locally refine cells based on flow properties and established cell difference thresholds. Owing to the highly transient shock-flame interactions and the absence of well-established subgrid models for detonation phenomena, no turbulence model was employed in the present simulations. Turbulent flow structures were therefore resolved directly to the extent permitted by the computational mesh, rather than modelled using Large Eddy Simulation (LES) or Reynolds-Averaged Navier-Stokes (RANS) approaches.

PeleC was chosen as it implements AMR directly out of the box, and for its inclusion of Riemann solvers to handle shock interactions. The appeal is that computational resources can be directed to the flame front specifically for a better management of the available resources.

The chemical mechanism employed in the simulations was the reduced ethylene oxidation mechanism developed by He et al. [36]. The mechanism was derived from the detailed USC II mechanisms and reduced to 26 species and 55 reactions. It was developed specifically for ethylene detonation simulations and was selected to reduce the computational cost associated with detailed chemistry while retaining the reaction pathways necessary to reproduce important detonation characteristics.

Single-step and simplified global reaction mechanisms are frequently employed in reac-

tive flow simulations of DDT because of their low computational cost [70, 99, 75]. However, such mechanisms may not adequately reproduce the unsteady chemical processes important to detonation initiation and failure. The reduced mechanisms of He et al. was therefore selected as a compromise between the computational cost of detailed chemistry and the chemical fidelity required for the present simulations.

3.2 Governing Equations

The governing equations consisted of conservations laws for mass, species, momentum, and total energy coupled with a finite rate chemical kinetics. PeleC solves that compressible reacting Navier-Stokes equations in conservative form:

$$\frac{\partial}{\partial t}(\rho) + \nabla \cdot (\rho \mathbf{u}) = 0 \tag{1}$$

$$\frac{\partial}{\partial t}(\rho Y_k) + \nabla \cdot (\rho \mathbf{u} Y_k) = -\nabla \cdot \mathcal{F}_k + \rho \dot{\omega}_k \tag{2}$$

$$\frac{\partial}{\partial t}(\rho \mathbf{u}) + \nabla \cdot (\rho \mathbf{u} \otimes \mathbf{u}) + \nabla p = \nabla \cdot \prod \tag{3}$$

$$\frac{\partial}{\partial t}(\rho E) + \nabla \cdot (\rho \mathbf{u} E + p \mathbf{u}) = \nabla \cdot \mathcal{Q} + \sum_k \rho q_k \dot{\omega}_k \tag{4}$$

Here ρ, $\mathbf{u}$, and p denote density, velocity and pressure respectively. Y_k is the mass fraction of the kth species. The total energy per unit mass is denoted by E and $\dot{\omega}_k$ is the chemical production rate. Diffusive transport is modeled through the species flux $\mathcal{F}_k$ (mixture averaged diffusion), thermal conduction flux $\mathcal{Q}$, and the viscous stress tensor $\prod$, given by:

where η and κ are the dynamic and bulk viscosity, respectively.

$$\prod = \eta(\nabla \mathbf{u} + (\nabla \mathbf{u})^T) + (\kappa - \tfrac{2}{3}\eta)\mathbf{I}\nabla \cdot \mathbf{u} \quad (5)$$

3.3 Computational Domain and Geometry

The referenced experimental domain was 560 $mm \times 30$ $mm \times 30$ mm consisting of an 80 mm smooth wall length for the development of the flame, followed by a 360 mm length consisting of two porous walls on top and bottom, and finally a 120 mm smooth wall length at the end.

To estimate the domain length required, the database of DDT experiments in unobstructed tubes that was produced by Mejia [72] was used. A directly comparable experiment was not identified in the database as the reported experiments did not align on all factors of geometry, initial pressure and temperature, or equivalence ratio. Mejia produced run-up distance models as an improvement to the previous models made by Dorofeev and Silverstrini [96, 24]. Mejia's model were used for a first estimate of the domain length. This produced an estimated distance of $1.5m$ which was deemed an unreasonable domain length due to the computational resources and run time required. As Lin reported an observed experimental run-up distance of only $13.5cm$, a domain length was chosen on the same order of distance. Computational domains employed were rectangular prisms with $240mm \times 30mm \times 15mm$ and $420mm \times 30mm \times 15mm$.

3.4 Mesh, Boundary and Initial Conditions

PeleC is built on the AMReX framework which uses a block structured mesh. This means that for each cell $dx = dy = dz$. The $240mm$ in length domain was discretized as $1024 \times 128 \times 64$ cells, and the $420mm$ in length domain was discretized as $1792 \times 128 \times 64$ cells. Number of cells was chosen to maintain the same cell size. The selected discretization resulted in a cell size of $\approx 0.234mm$. PeleC groups the cells in the simulation domain into a hierarchy of rectangular grids called boxes which are eight cells in length, width, and height. The solver tags cells that require higher resolution on the basis of a threshold of the gradient of the neighbouring cells. When a cell is tagged for refinement, the entire box containing that cell is refined. For these simulations, a refinement ratio of two was employed in each spatial direction, such that each three-dimensional cell within the refined box was subdivided into eight cells.

For the present simulations, cells were tagged for refinement based on cell-to-cell differences in temperature and pressure. Thresholds of 1000 K and 50 kPa between neighbouring cells were selected through preliminary simulations. The flame front produced a sufficiently sharp temperature change to be captured over the range of temperature thresholds tested; however, lower thresholds caused refinement to extend farther into the burned gases behind the flame front, unnecessarily increasing the refined volume. Similarly, lower pressure thresholds resulted in refinement being triggered by the initial pressure perturbations produced during ignition. The selected thresholds therefore provided refinement around the propagating flame front and developing shock wave while limiting refinement elsewhere in the domain to manage computational cost.

Three levels of AMR were used for the 0 and 10 PPI cases, while four levels of AMR were used for the higher-resolution 10 PPI simulation. An additional 10 PPI simulation employing two levels of AMR was performed for the grid sensitivity analysis described in Section 4.1, with the results presented in Chapter 4. A summary of the simulated cases can be found in Table 3.1, and the AMR cell sizes can be found in Table 3.2. The finest levels of refinement have a cell size of $15\mu m$ which was chosen based on the work of Crane et al.[18] in which a numerical study of detonation in confinement was able to achieve $10\mu m$ resolution. The works of Crane et al. simulated a domain of $12mm \times 12mm \times 12mm$ and thus a system with AMR was used to expand the resolution to a large domain for this study.

Case	Pore Density	Domain Length (mm)	Max AMR level
Null_Case	0 PPI	420	3
10PPI_2AMR	10 PPI	240	2
10PPI_3AMR	10 PPI	240	3
10PPI_4AMR	10 PPI	240	4

Table 3.1: Summary of simulated cases

AMR Level	Cell size
0	0.234 mm
1	0.117 mm
2	0.059 mm
3	0.029 mm
4	0.015 mm

Table 3.2: AMR level cell sizes

PeleC boundary conditions (BCs) are grouped as (x_{lo} y_{lo} z_{lo}) and (x_{hi} y_{hi} z_{hi}). No slip walls were used for x_{lo} and an outlet was used for x_{hi}. No slip walls were used for

y_{lo} and y_{hi} for the first $80mm$ of the domain length, and then custom BCs were used for the remainder of the domain. A symmetry plane was used at z_{lo} and no slip walls were used for z_{hi}. The custom BCs consisted of a repeated circular pores with the previously mentioned pore densities of 0 PPI (null case, no pores) and 10 PPI. The pores acted as outlets and between the pores were no slip walls. It should be noted that neither Jiang [41] nor Lin [62] specified the porosity of their copper foam, as such multiple copper foam manufacturers were surveyed and the porosity of their advertised stock was averaged at $\approx$ 80%. This resulted in a pore diameter $1.8mm$ for the 10 PPI case. The circular pores were arranged in a regular hexagonal pattern because the maximum porosity that can be achieved with a rectangular pattern is $\approx$ 73%. All outlet boundaries, including the pores and the downstream domain boundary, were treated using PeleC's first-order extrapolation outflow boundary condition. The conserved variables were extrapolated from the interior domain into the boundary ghost cells, after which the primitive variables, including pressure, were evaluated from the extrapolated conserved state. Therefore, no static pressure was prescribed at the pore outlets. The boundary conditions can be seen in Figures 3.1 and 3.2.

The simulation was initialized with a quiescent stoichiometric mixture of ethylene and oxygen C_2H_4+$3O_2$ at a temperature of 300 K and a pressure of 1 atm. Ignition was achieved using a volumetric energy source corresponding to an approximately 0.1 J spark, applied over a radius of 1 mm for 2 μs. The ignition source was centred at $(x, y, z) = (0, 0, 0)$, corresponding to the centre of the closed end wall in the full experimental domain. This differs from the experiments, in which ignition was provided by a spark plug embedded in the side wall. The energy deposition produced a flame kernel at approximately 2250 K,

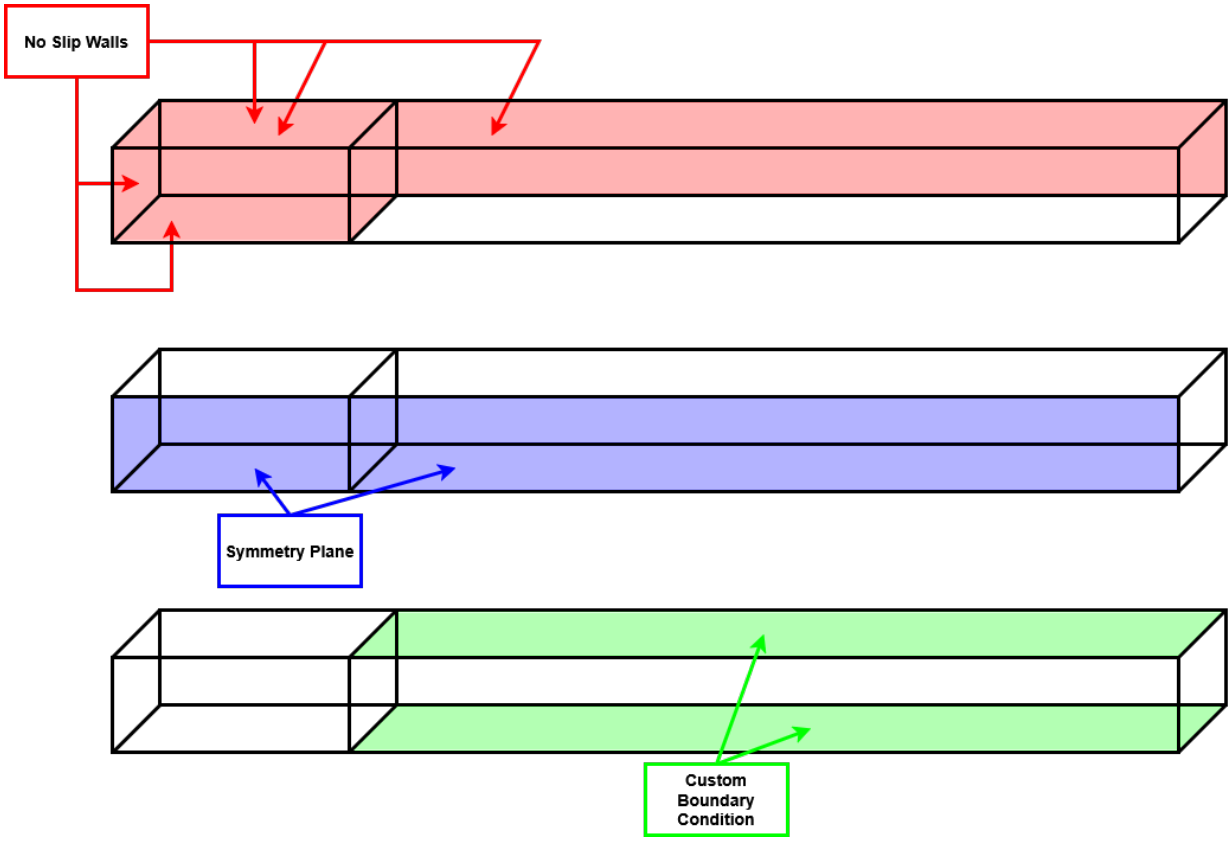

Figure 3.1: Boundary conditions

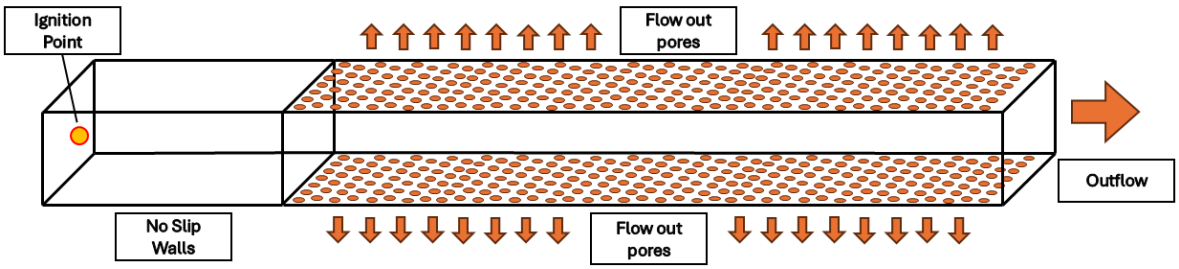

Figure 3.2: Custom porous wall boundary condition

which subsequently ignited the surrounding mixture and produced the propagating flame.

The 3AMR simulations were run on 9,216 processors for one week at a time for an approximate total of 1.5 million core hours per simulation. The 4AMR simulation was run on 25,088 processors for multiple weeks, taking a total of approximately 12.2 million core hours.

3.5 Post-processing and Data Analysis

This section contains the methods used for data extraction and the analysis to produce the results presented in Chapter 4: Results. The section is broken down into the method used for the extraction of simulation data, the visualization of the data, and the subsequent detection of the flame front for the flame speed calculations, and the detection of the developing shock front.

3.5.1 Extraction of Simulation Data

The simulation data was extracted using the ytScripts library created by Nick Wimer as can be found at `nickwimer.github.io/ytScripts/`. This Git repository is built upon the yt Project [101] library for data set visualization. The code was modified to allow for the extraction of multiple data fields into one dataset to accelerate the post processing workflow.

Data subsets were extracted from the simulation as planar slices. xy plane slices were taken near the symmetry boundary at the core of the simulated domain and near the wall

of the domain. For simulations that included pores on the y boundaries, the xy slices were taken such that they intersected with the centre of a row of pores so that the impact of the pores could be visualized. xz plane slices were taken near one of the custom pore boundaries. Slices near the walls were slightly offset from the wall to prevent no slip conditions from imposing a zero velocity at the plane. The slice locations can be seen in Table 3.3 and visualized in Figure 3.3.

Case	Core z-pos (xy plane)	Wall z-pos (xy plane)	Wall y-pos (xz plane)
Null	$-0.1cm$	$-1.48cm$	$1.49cm$
10 PPI	$-0.22cm$	$-1.48cm$	$1.49cm$

Table 3.3: Planar slice positions in centimeters

3.5.2 Visualization

Initial visualization was performed using ParaView 5.13.3 on the Trillium HPC cluster. As the simulation progressed, AMR concentrated cells around the expanding flame front. In the 10PPI 4AMR simulation, the mesh reached approximately 1×10^9 cells, resulting in datasets that exceeded the practical interactive visualization capabilities of ParaView, despite using eight processing cores and 1 TB of system memory. Consequently, two-dimensional slices were then extracted as described in Section 3.5.1 for visualization.

The slices were visualized using custom Python scripts employing Matplotlib [39]. Temperature, pressure, density, velocity, and vorticity were plotted for each extracted slice, with pore locations overlaid to provide geometric context. Sequential images were compiled into animations that facilitated qualitative assessment of flame propagation.

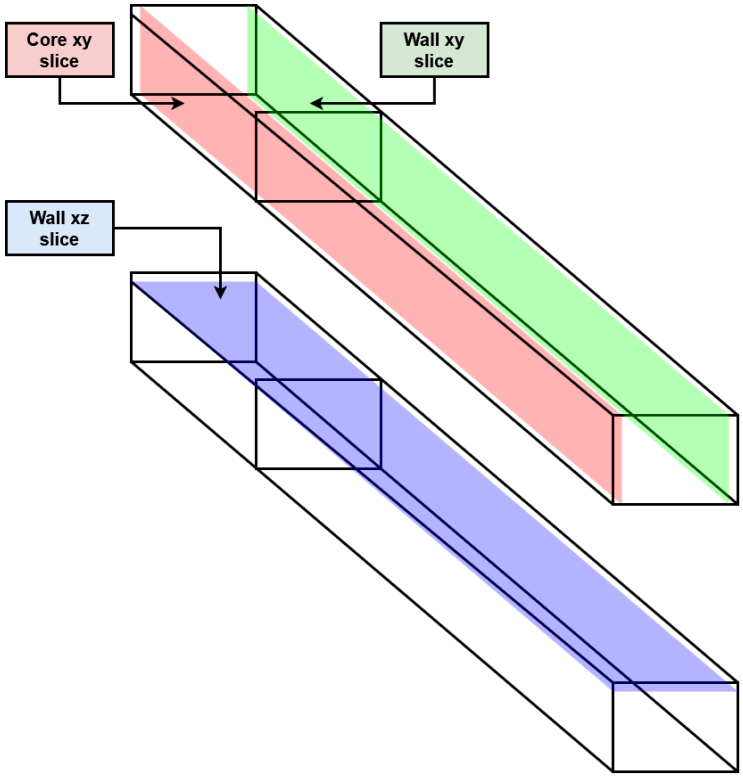

Figure 3.3: Slice locations and orientations

3.5.3 Flame Front Detection and Flame Speed

To quantify flame propagation, custom Python scripts were developed to identify the flame front from the extracted temperature slices. A threshold temperature of 1500 K was used to delineate the burned and unburned mixtures, with the temperature field evaluated row-by-row. The propellant mixture was initialized at 300 K, while the adiabatic flame temperature of ethylene-oxygen combustion exceeds 2000 K when accounting for energy losses due to product dissociation. A threshold of 1500 K therefore provided a clear distinction between the burned and unburned mixtures while remaining sufficiently below the

peak flame temperature.

Flame detection is estimated by identifying the foremost axial location at which the temperature threshold was exceeded. However, the flame front exhibited significant local wrinkling and turbulence, resulting in localized protrusions that produced frame-to-frame fluctuations in the detected flame position. To obtain a more representative measure of bulk flame propagation, a second flame position was defined as the axial location at which at least 30% of the cross-sectional area had exceeded the temperature threshold. This criterion reduced the influence of localized flame protrusions while preserving the overall propagation behaviour of the flame.

The 30% criterion was particularly beneficial for the near-wall measurements. As the flame interacted with the porous boundary layer, combustion products initially appeared as isolated high-temperature regions before the bulk flame advanced downstream. Tracking only the foremost detected location therefore produced an erratic estimate of the flame position, whereas the cross-sectional criterion provided a smoother and more representative measurement of flame propagation. In addition to the leading-edge and bulk flame locations, the point at which the flame first intersected the porous boundary layer was also recorded. Examples of the flame detection algorithm are shown in Figures 3.4 and 3.5, which can be found below.

The detected flame positions were ordered according to their corresponding simulation time, and the flame speed was calculated using a first-order finite difference,

$$S_f = \frac{x_{i+1} - x_i}{t_{i+1} - t_i}, \tag{3.1}$$

where S_f is the flame speed, x is the detected flame front location, and t is the corresponding simulation time. This procedure was applied to both the leading-edge and bulk flame front measurements to quantify flame propagation throughout the simulations.

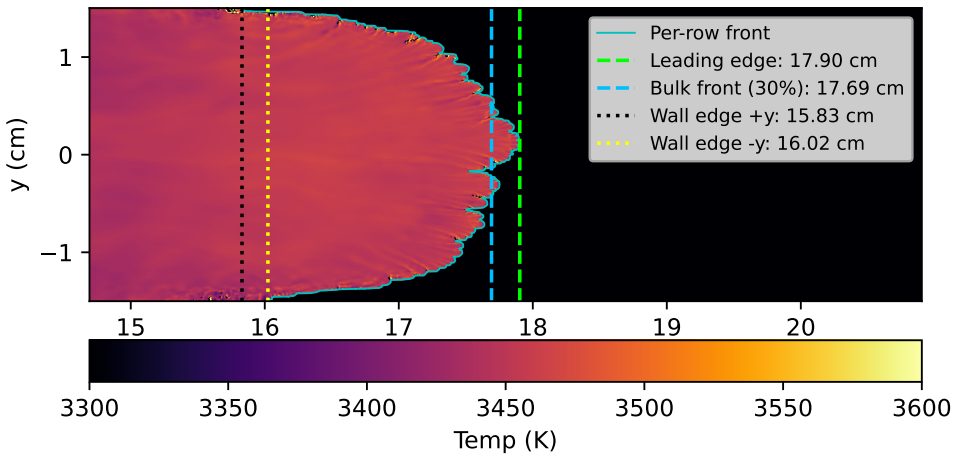

Figure 3.4: Example of flame front detection within the core flow.

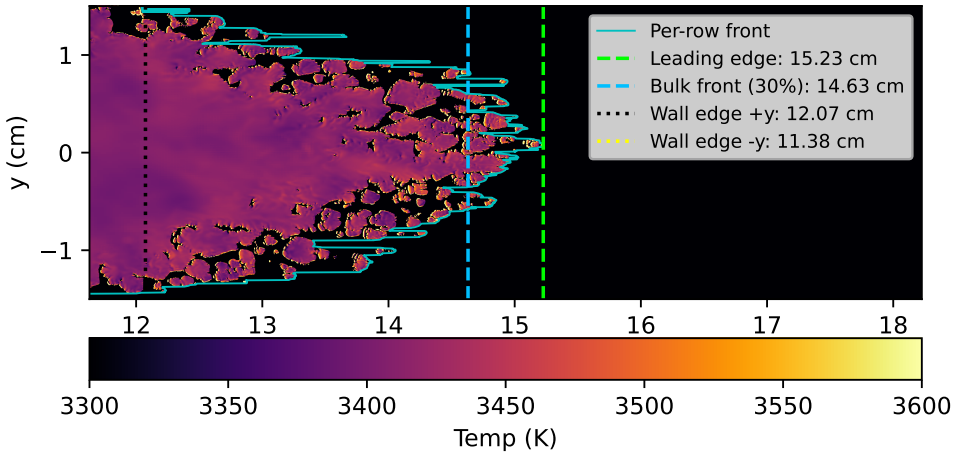

Figure 3.5: Example of flame front detection near the porous wall boundary.

3.5.4 Shock Wave Detection and Shock Strength

As discussed in previous chapters, shock formation occurs ahead of the developing flame. As the flame accelerates, pressure waves generated ahead of the flame coalesce and progressively steepen. Prior to the formation of a defined shock, this produces a broad pressure rise ahead of the flame rather than a sharp pressure discontinuity. As wave steepening continues, this pressure rise develops into a defined shock wave. In the case of the porous system, energy is taken out of the system via the pores, which is expected to delay the wave steepening into a shock.

Python scripts were written to extract pressure data and identify the formation of a shock. A one-dimensional pressure profile was extracted along the centre-line of the domain to characterize the developing pressure wave. The front and rear of the wave were defined using a windowed percent of the peak pressure with 5% used as the criteria. Therefore the front was detected as a pressure rise of 5% of the peak global pressure, and the rear was detected as 95% of the peak global pressure. This was chosen to separate the front of the building pressure wave from the pressure perturbations that preceded the wave, and to separate the rear of the wave from pressure fluctuations after the wave had plateaued.

To identify shock formation, the row-averaged pressure profile was smoothed over a fixed physical width of 0.0135 cm before calculating the spatial pressure gradient. A shock was considered to have formed when the maximum pressure gradient exceeded 2 MPa/cm. This threshold was selected through inspection of the temporal pressure profiles such that detection corresponded to the emergence of a distinct, abrupt pressure rise of approximately 1 atm in magnitude, while excluding the more gradual pressure gradients associated

with the developing compression wave. The same physical smoothing length and gradient criterion were applied consistently to all simulation cases.

The code identifies the front and rear of the developing pressure wave as described and then switches when the shock criteria is met to detecting the shock front. When the shock criteria is met the shock strength is taken as the pressure ratio across the cells at either end of the shock window. Examples of the shock detection can be seen in Figures 3.6 and 3.7.

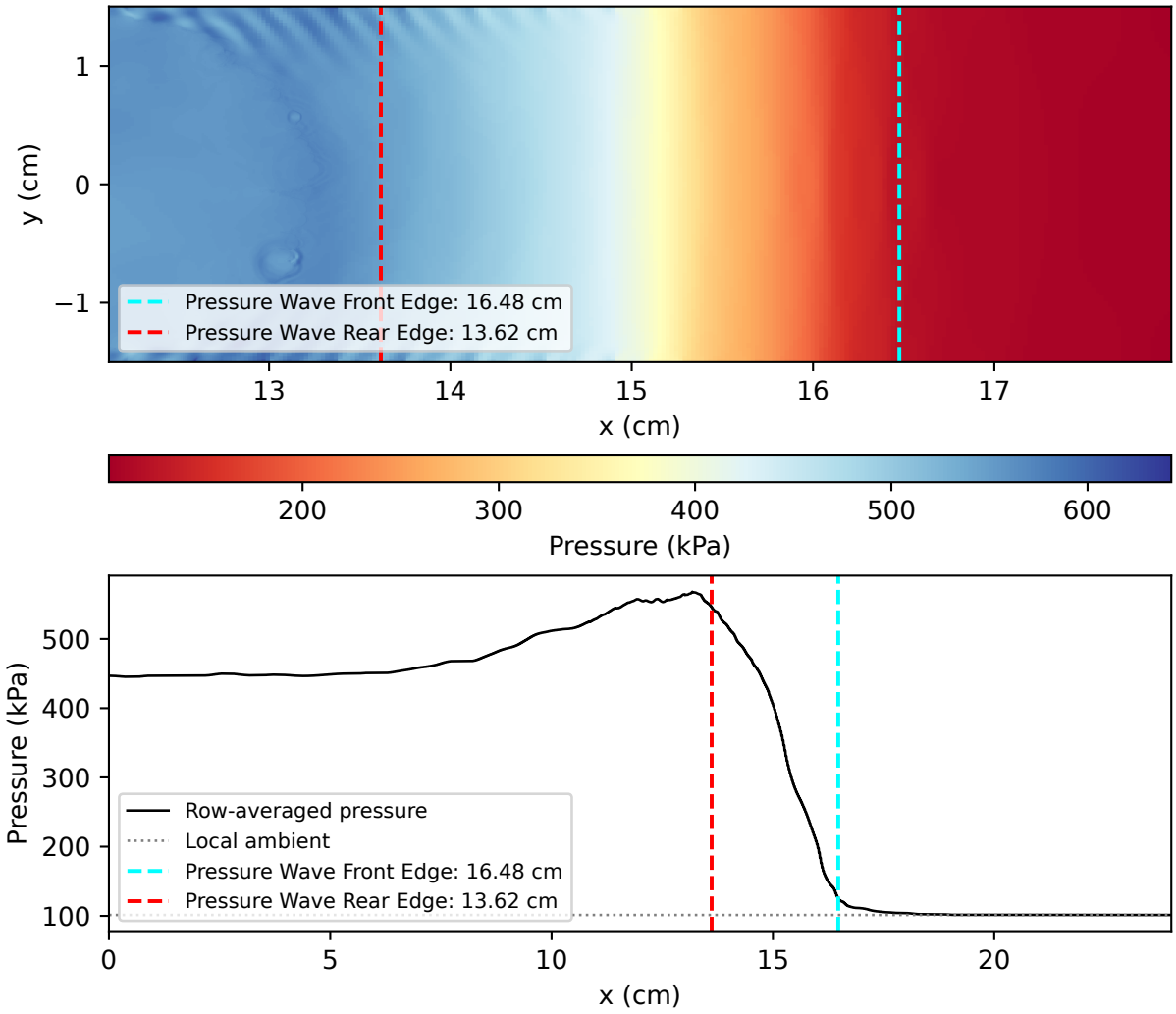

Figure 3.6: Examples of shock detection of developing pressure wave. Top: Zoomed region of the detected wave, Bottom: row averaged pressure profile

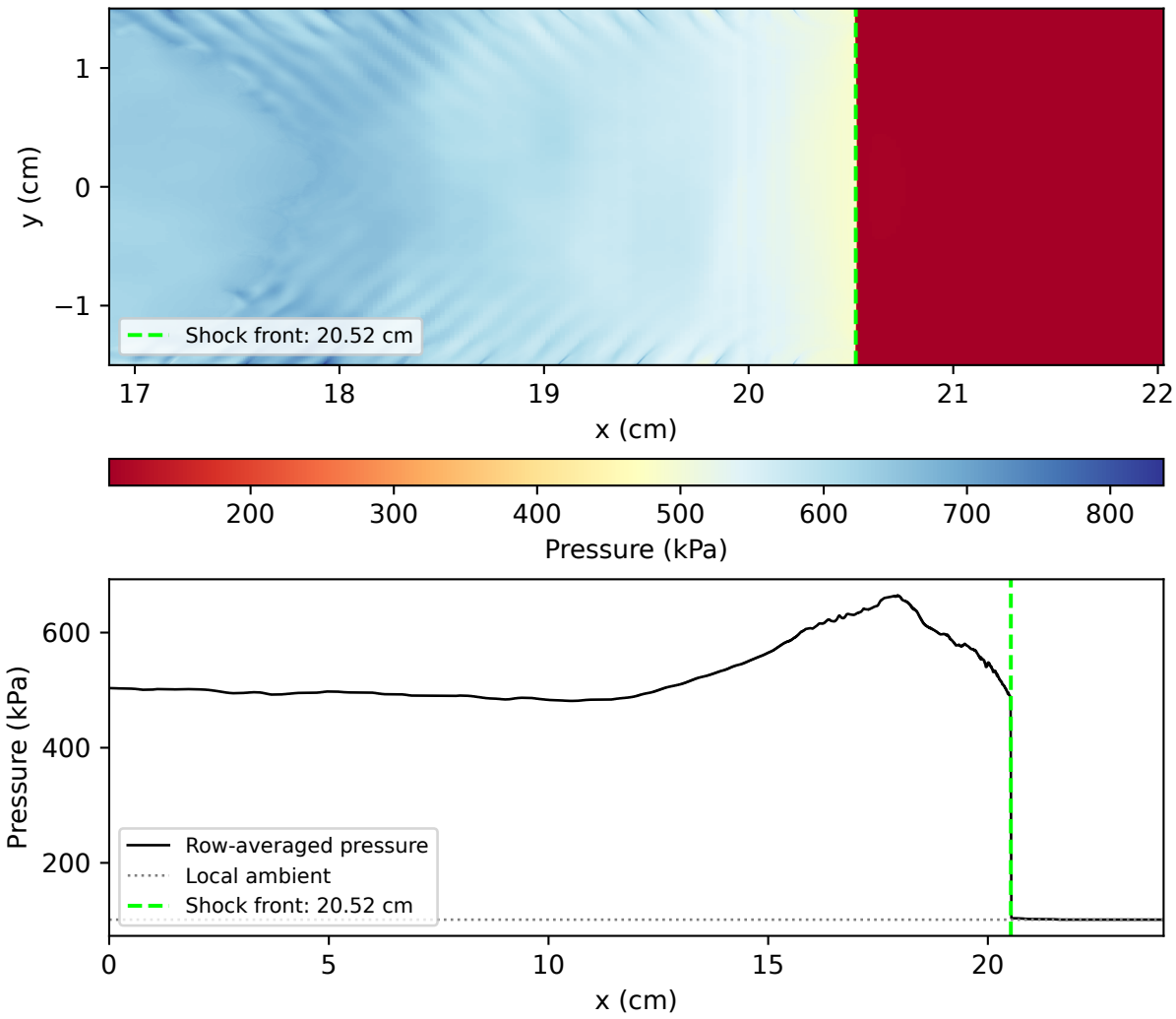

Figure 3.7: Example of shock detection of formed shock wave. Top: Zoomed region of the detected wave, Bottom: row averaged pressure profile

3.5.5 Grid Sensitivity Analysis

A grid sensitivity analysis was performed using the 10 PPI configuration at maximum AMR levels of 2, 3, and 4. The bulk flame velocity was selected as the primary quantity

of interest because it directly characterizes the flame acceleration behaviour examined in this study. It was captured using the methods outlined in subsection 3.5.3. Since the flame position was sampled at different axial locations in each simulation, the velocity data from each AMR level were first linearly interpolated onto a common spatial coordinate prior to comparison.

The quantitative comparison was restricted to the axial interval from 4 to 10 cm. The initial region near the ignition source was excluded in order to reduce the influence of the ignition transient and allow the comparison to focus on the subsequent flame acceleration. The upper bound was selected such that all three simulations contained data over the complete comparison interval.

The difference between successive AMR levels was quantified using a normalized integrated absolute difference in bulk flame velocity,

$$\epsilon_{i \to j} = \frac{\displaystyle\int_{x_1}^{x_2} |U_i(x) - U_j(x)| \, dx}{\displaystyle\int_{x_1}^{x_2} |U_j(x)| \, dx} \times 100\%, \tag{3.2}$$

where $U_i(x)$ and $U_j(x)$ are the bulk flame velocities for two successive AMR levels, with the finer simulation j used as the reference. The limits of integration were $x_1 = 4$ cm and $x_2 = 10$ cm. Accordingly, the 2AMR simulation was compared with the 3AMR simulation, and the 3AMR simulation was compared with the 4AMR simulation.

The integrated metric was selected instead of a pointwise percentage difference because the flame velocity was calculated from discrete changes in detected flame position and therefore exhibits short-scale fluctuations. Integration over the common spatial interval

reduces the influence of individual local variations while preserving differences in the overall flame acceleration behaviour. The metric was evaluated in 1 cm intervals over the comparison region of $4 - 10$ cm.

Chapter 4

Results

This chapter presents the results of the numerical simulations of the initiation of detonation based on the methodology presented in Chapter 3. These results are presented as observations, while the interpretation of these findings is reserved for Chapter 5, Discussion. The exception is Section 4.1, Grid Sensitivity Study, which evaluates the sensitivity of the predicted flame propagation to grid refinement and establishes the limitations associated with comparing simulations performed at different levels of AMR.

4.1 Grid Sensitivity Study

In order to assess grid sensitivity, the 10 PPI configuration was simulated using maximum AMR levels of 2, 3, and 4 and analyzed according to the methodology described in Section 3:3.5.5. The bulk flame velocity as a function of flame front position for each simulation is shown in Figure 4.1.

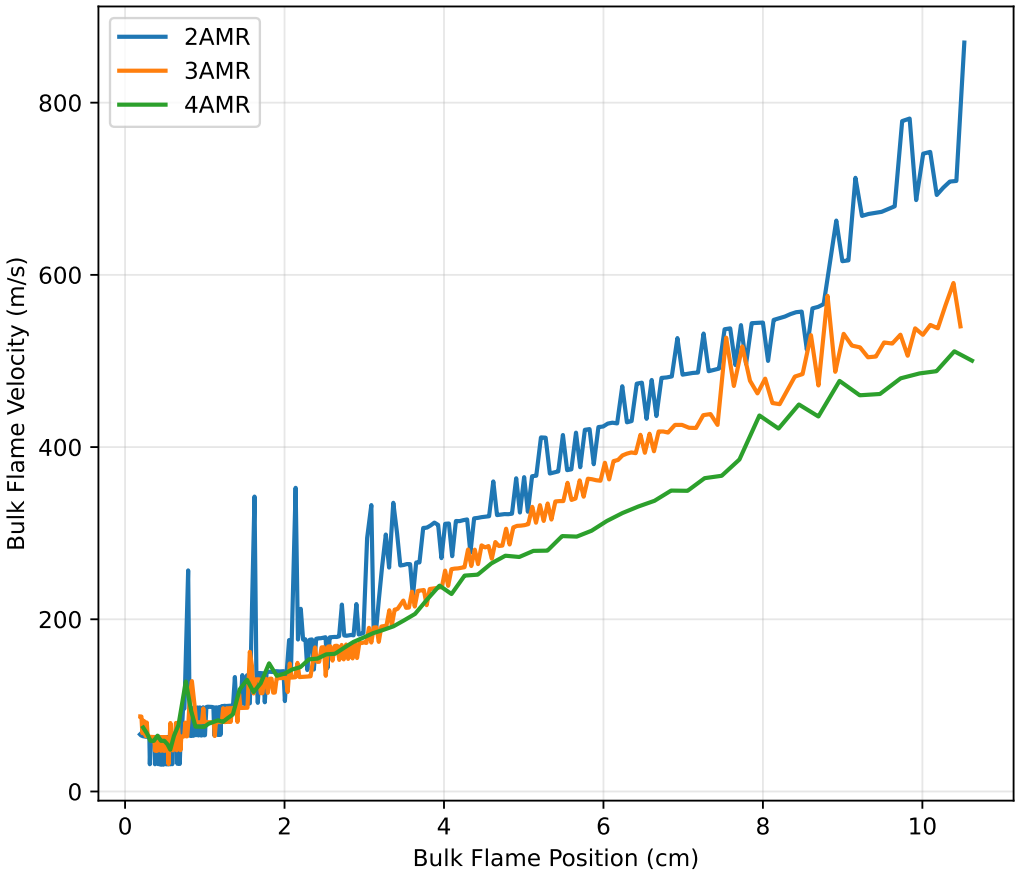

Figure 4.1: Bulk flame velocity as a function of flame front position for the 2AMR, 3AMR, and 4AMR simulations

Within the 4–10 cm comparison region, differences in the flame acceleration become apparent between the three AMR levels. The 2AMR simulation exhibits greater short-scale variation in the calculated flame velocity and generally accelerates more rapidly than the higher-resolution simulations. The 3AMR simulation exhibits less short-scale variation than the 2AMR simulation, but generally predicts a higher flame velocity than the 4AMR simulation. The differences between successive AMR levels over 1 cm intervals are

presented in Table 4.1.

Position Interval (cm)	2AMR–3AMR Difference (%)	3AMR–4AMR Difference (%)
4–5	14.68	8.45
5–6	14.60	16.37
6–7	14.40	20.61
7–8	11.09	21.47
8–9	15.07	10.86
9–10	33.51	10.23

Table 4.1: Normalized integrated differences in bulk flame velocity over 1 cm intervals

The interval comparison demonstrates that the change between successive AMR levels is not uniform throughout the domain. Between 4 and 5 cm and between 8 and 10 cm, the difference between the 3AMR and 4AMR simulations is smaller than that between the 2AMR and 3AMR simulations. Conversely, between 5 and 8 cm, the 3AMR-4AMR difference exceeds the 2AMR-3AMR difference.

Over the complete 4–10 cm interval, the normalized integrated difference decreases from 17.96% between the 2AMR and 3AMR simulations to 14.52% between the 3AMR and 4AMR simulations, as summarized in Table 4.2. This corresponds to a 19.14% reduction in the difference between successive AMR levels.

Simulation Comparison	Normalized Integrated Difference (%)
2AMR-3AMR	17.96
3AMR-4AMR	14.52

Table 4.2: Normalized integrated differences in bulk flame velocity over the complete 4–10 cm interval

The results demonstrate reduced overall grid sensitivity with increasing refinement; however, the non-monotonic behaviour observed over individual spatial intervals indicates

that grid-independent behaviour has not been demonstrated. Further refinement would be required to establish grid convergence, but the computational cost associated with the 4AMR simulation makes an additional AMR level impractical for the present study. The 4AMR simulation is therefore used for the highest-resolution qualitative analysis of the flame and flow structure, while quantitative comparisons between the porous and non-porous configurations use the 10PPI 3AMR and Null 3AMR simulations, which employ equivalent maximum AMR levels. This is considered acceptable because the 10PPI 3AMR and 4AMR simulations exhibit similar trends in flame acceleration and progressively diverge from the behaviour of the 2AMR simulation, providing confidence that the 10PPI 3AMR and Null 3AMR simulations can be used for quantitative comparison.

4.2 Flame Evolution

This section presents the visual evolution of the flame. Three simulations were conducted, each producing a series of plot files from which three slices containing seven fields were extracted: temperature, pressure, X velocity, Y velocity, velocity magnitude, vorticity magnitude, and density. The number of output plot sets and corresponding simulation time for each case are presented in Table 4.3. Visualization of the data is presented in the form of smear plots of the temperature and pressure fields, representing the evolution of the flame front and the formation of a shock.

The temperature and pressure fields are used to examine the spatial and temporal development of the flame and leading pressure wave. Core temperature is used to characterize the bulk flame evolution, while the pressure field is used to examine the development

Case	Number of Output Plot Sets	Time Represented	Flame Distance Achieved
3AMR Null	264	496.062 μs	$\approx$ 14.8 cm
3AMR 10PPI	322	564.596 μs	$\approx$ 11.7 cm
4AMR 10PPI	143	650.047 μs	$\approx$ 17.9 cm

Table 4.3: Distribution of Collected Data

and steepening of the leading pressure wave as the flame accelerates. Local interactions between the flame and porous boundary are examined separately in Section 4.5.

4.2.1 Null 3AMR Temperature and Pressure Smears

Figures 4.2 and 4.3 show the temporal evolution of the temperature and pressure fields, respectively, for the Null 3AMR simulation. The temperature field illustrates the development and propagation of the flame through the domain, while the pressure field shows the corresponding development and propagation of the pressure waves ahead of the flame. It can be noted that the Null case displays a plug flame with sharper corners and a pressure field that has reflected waves through the region between the flame front and developing shock front.

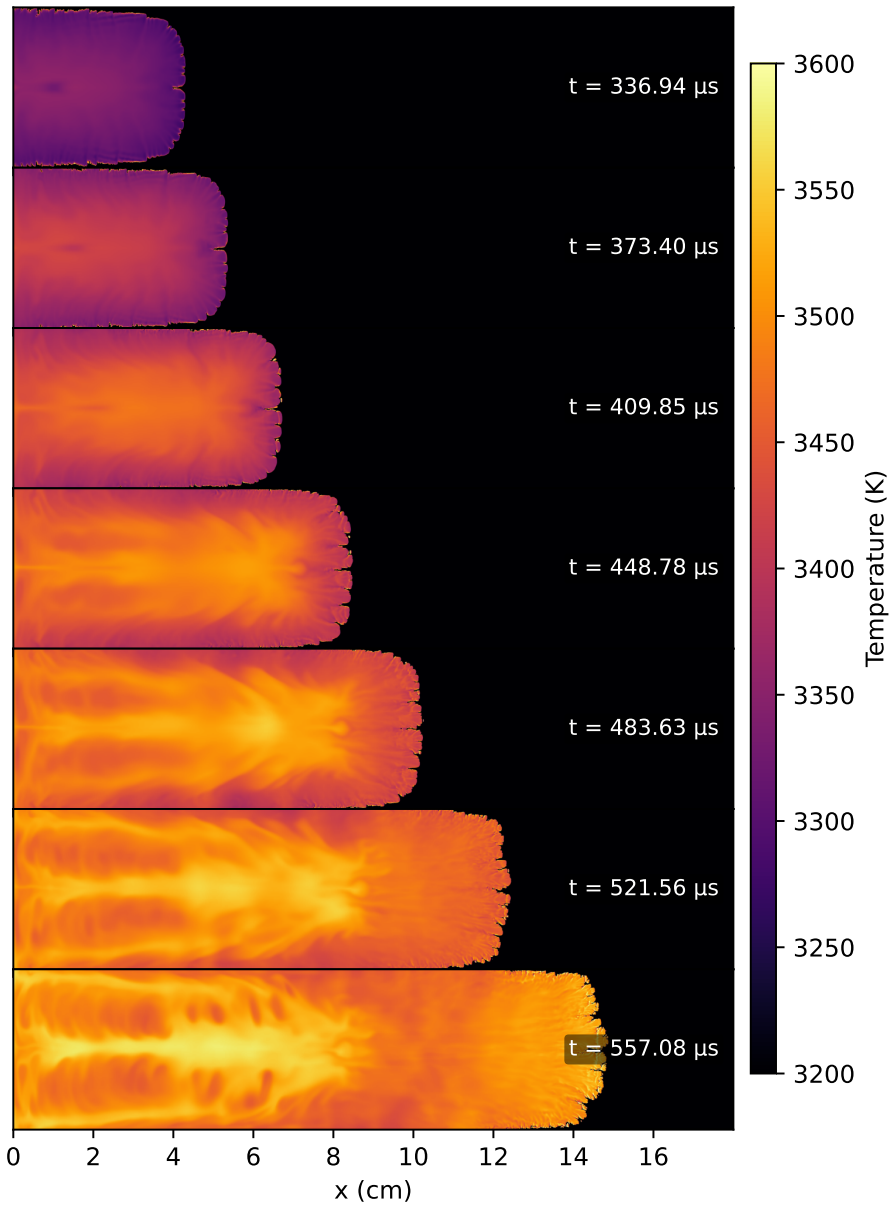

Figure 4.2: Flame smear from the core Null 3AMR

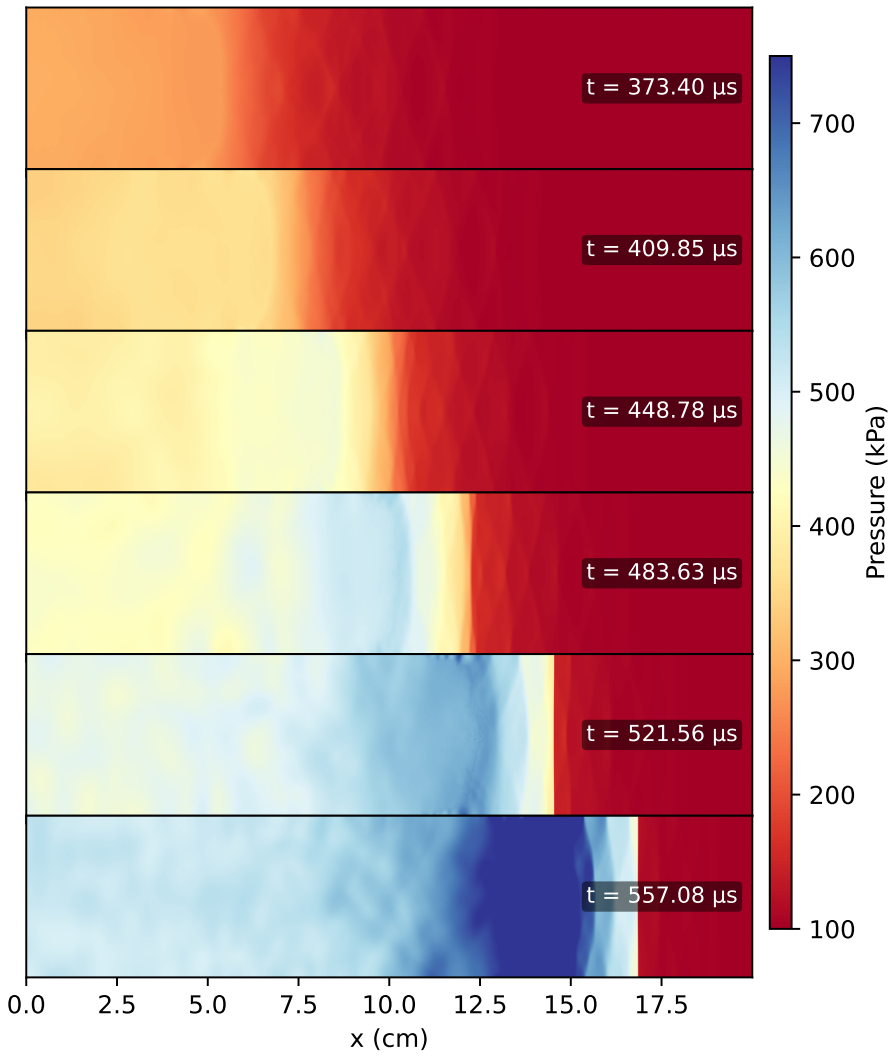

Figure 4.3: Pressure smear from the core Null 3AMR

4.2.2 10PPI 3AMR Temperature and Pressure Smears

Figures 4.4 and 4.5 show the temporal evolution of the temperature and pressure fields, respectively, for the 10PPI 3AMR simulation. The temperature field illustrates the devel-

opment and propagation of the flame through the domain, while the pressure field shows the corresponding development and propagation of the pressure waves ahead of the flame. The porous cases display a greater curvature in the corners of the flame front approaching the wall. The pressure field shows a weaker gradient between the flame front and the developing shock front.

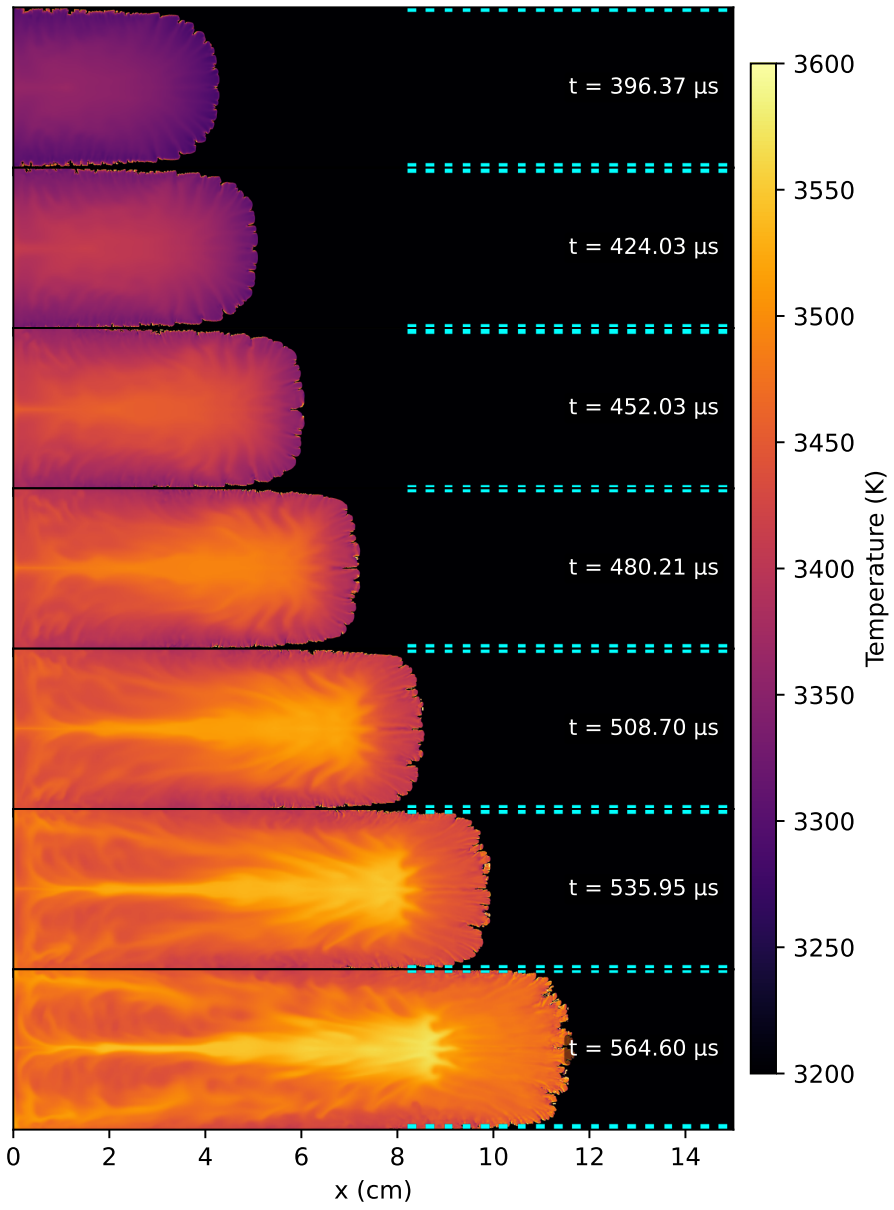

Figure 4.4: Flame smear from the core 10PPI 3AMR

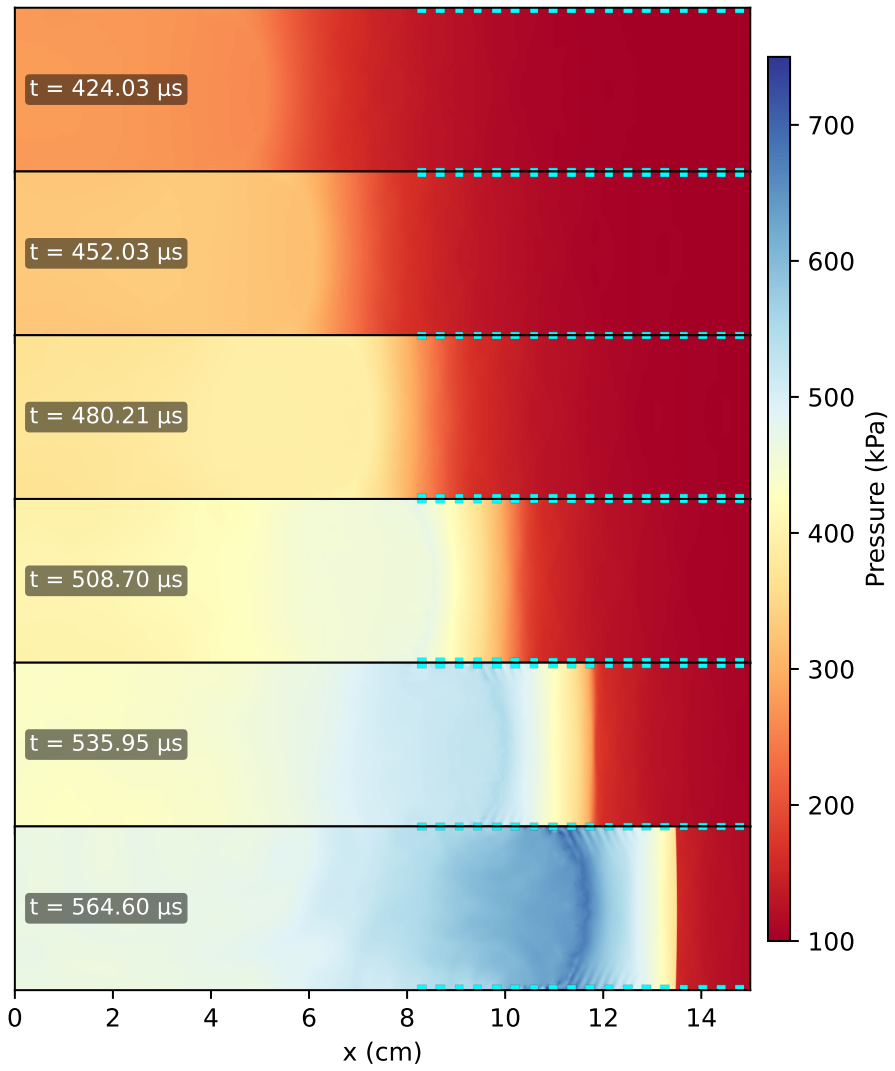

Figure 4.5: Pressure smear from the core 10PPI 3AMR

4.2.3 10PPI 4AMR Temperature and Pressure Smears

Figures 4.6 and 4.7 show the temporal evolution of the temperature and pressure fields, respectively, for the 10PPI 4AMR. The temperature field illustrates the development and

propagation of the flame through the domain, while the pressure field shows the corresponding development and propagation of the pressure waves ahead of the flame.

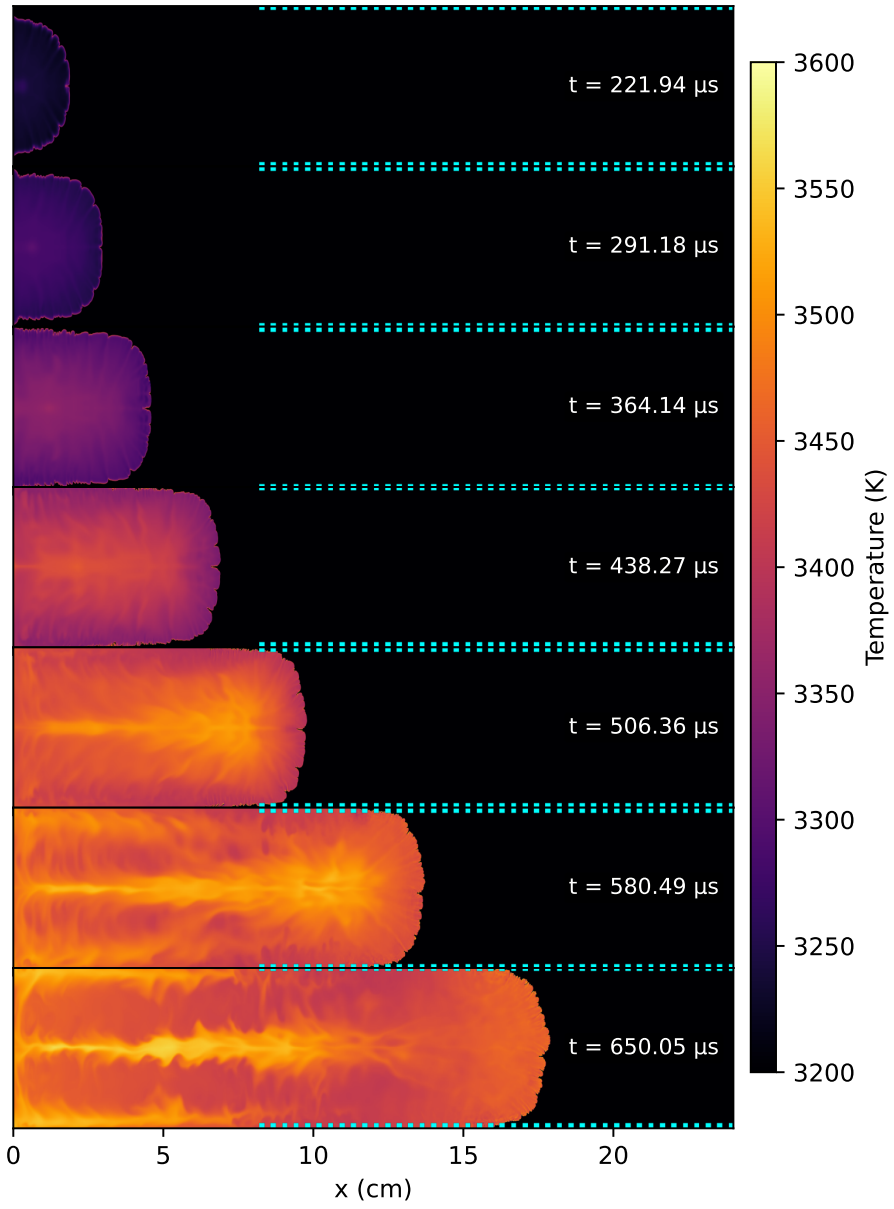

Figure 4.6: Flame smear from the core 10PPI 4AMR

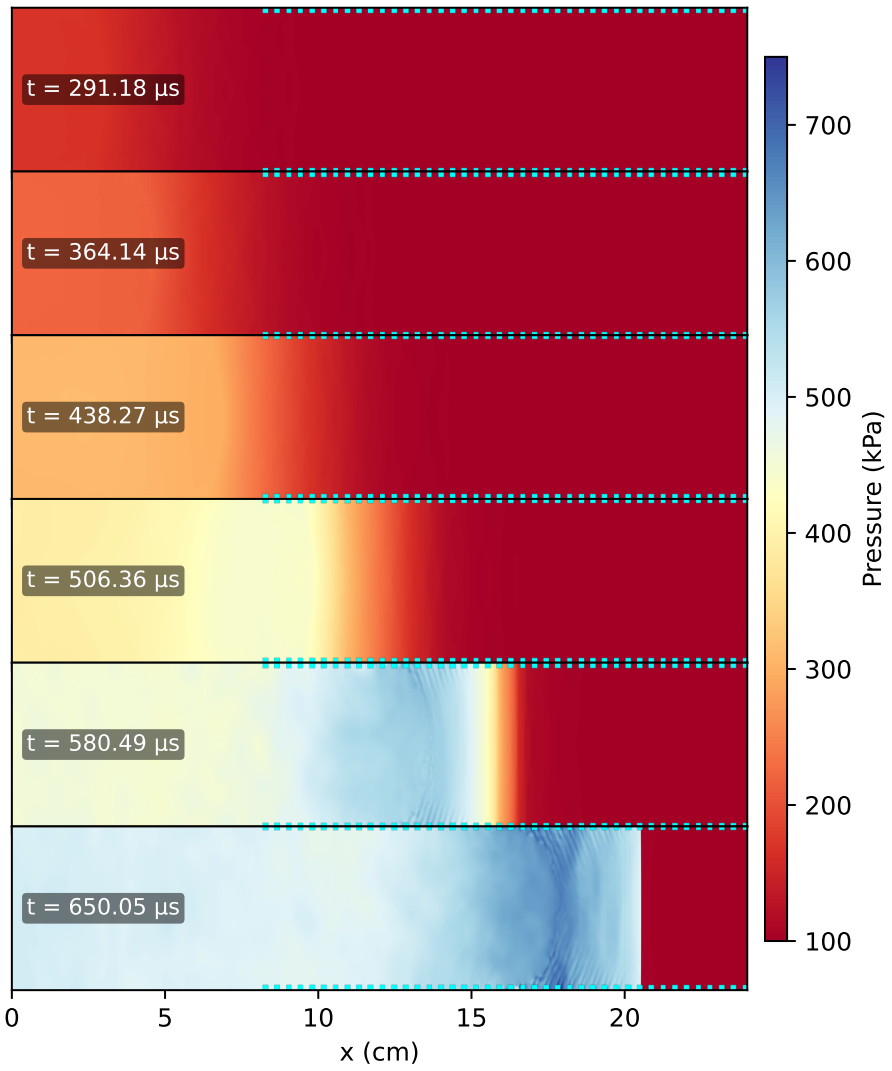

Figure 4.7: Pressure smear from the core 10PPI 4AMR

4.3 Flame Speed and Propagation

The extracted flame velocity profiles are presented in Figure 4.8 and compared with the experimental results reported by Lin et al. [62]. The numerical results include the Null 3AMR simulation and the 10PPI porous outlet simulations conducted with maximum AMR levels of 3 and 4.

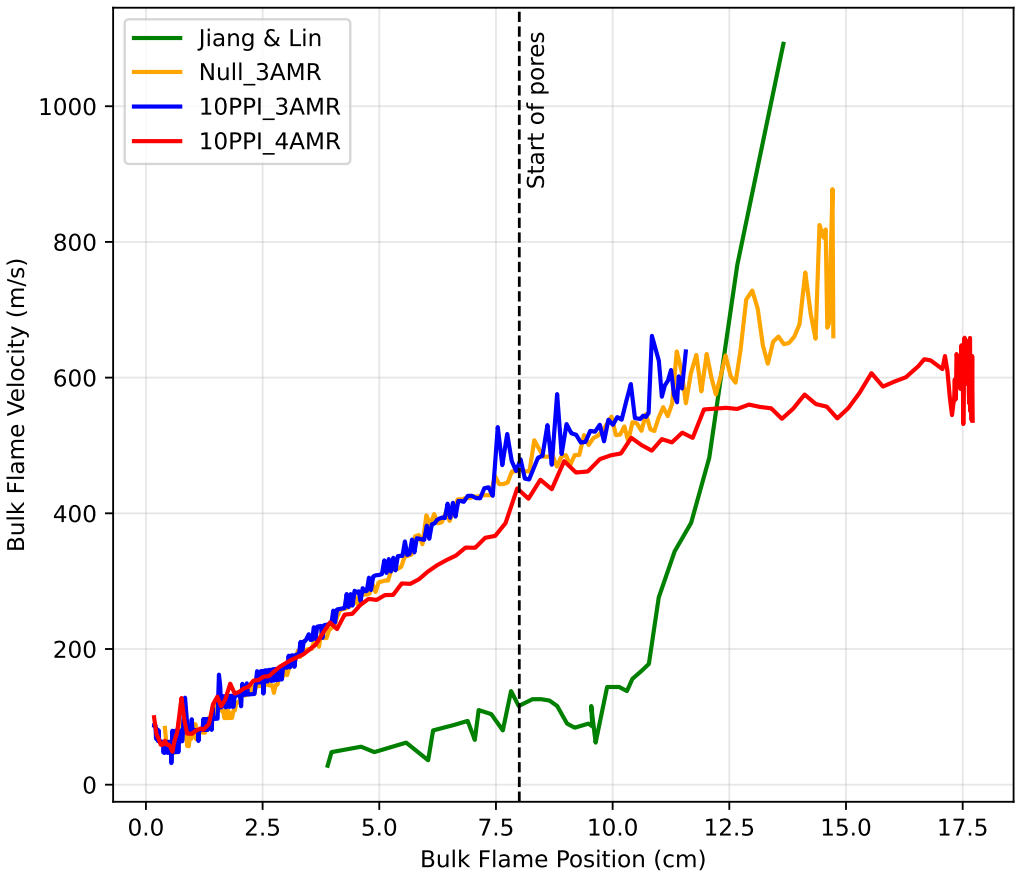

Figure 4.8: Comparison of the reported experimental flame velocity with the calculated bulk flame velocities of the Null 3AMR, 10PPI 3AMR, and 10PPI 4AMR simulations

Both 3AMR simulations exhibit similar increases in flame velocity as the flame propagates through the flame development section of the channel. The Null 3AMR and 10PPI 3AMR velocity profiles remain closely aligned through the available 10PPI 3AMR data, which extends to a bulk flame position of approximately 11.7 cm. This agreement persists after the porous outlet boundary begins at approximately 8 cm. In contrast, the 10PPI 4AMR simulation exhibits a lower flame velocity than both 3AMR simulations, with the separation becoming apparent before the flame reaches the porous section. The Null 3AMR simulation subsequently reaches a maximum velocity of approximately 850 m/s, while the 10PPI 4AMR simulation reaches approximately 630 m/s. None of the numerical simulations exhibit the rapid increase in flame velocity observed experimentally by Jiang and Lin during the later stages of flame acceleration.

4.4 Shock Formation and Pressure Profiles

Row averaged pressure profiles were extracted and presented in Figure 4.9 as a 3D plot. The x-axis represents the location along the x-domain that is truncated to $24cm$ in length, the y-axis represents the pressure in kPa, and the z-axis represents time in μs to show that depth into the plot illustrates the progression of time through the simulations. The simulations did not have the same frequency of data output for plot files and so 12 evenly spaced data sets are taken from the 10PPI 4AMR simulation, 11 data sets are from the 10PPI 3AMR, and 11 data sets are from the Null 3AMR simulation that are nearest to the appropriate time. For clarity, the peak pressures are denoted in the legend.

Figure 4.10 shows the evolution of the pressure wave and shock locations with time,

together with the corresponding pressure ratio. The pressure wave front progresses approximately linearly in both simulations, while the rear advances more rapidly as the pressure wave steepens. This behaviour results from the accelerating flame, as the rear of the pressure wave remains near the flame front. Consequently, the distance between the detected front and rear decreases as the pressure wave steepens toward the formation of a discontinuous shock. Greater fluctuations are observed in the rear edge of the Null 3AMR case due to the presence and interaction of multiple pressure waves during the development of the compression region. Both 10PPI cases exhibit smoother and delayed shock development relative to the Null 3AMR case. Despite the temporal delay, shock formation occurs at a similar axial location in the Null 3AMR and 10PPI 3AMR simulations. The peak pressures of the 10PPI 3AMR and 10PPI 4AMR cases are also similar, reaching approximately 657 kPa and 665 kPa, respectively, compared with approximately 738 kPa in the Null 3AMR case.

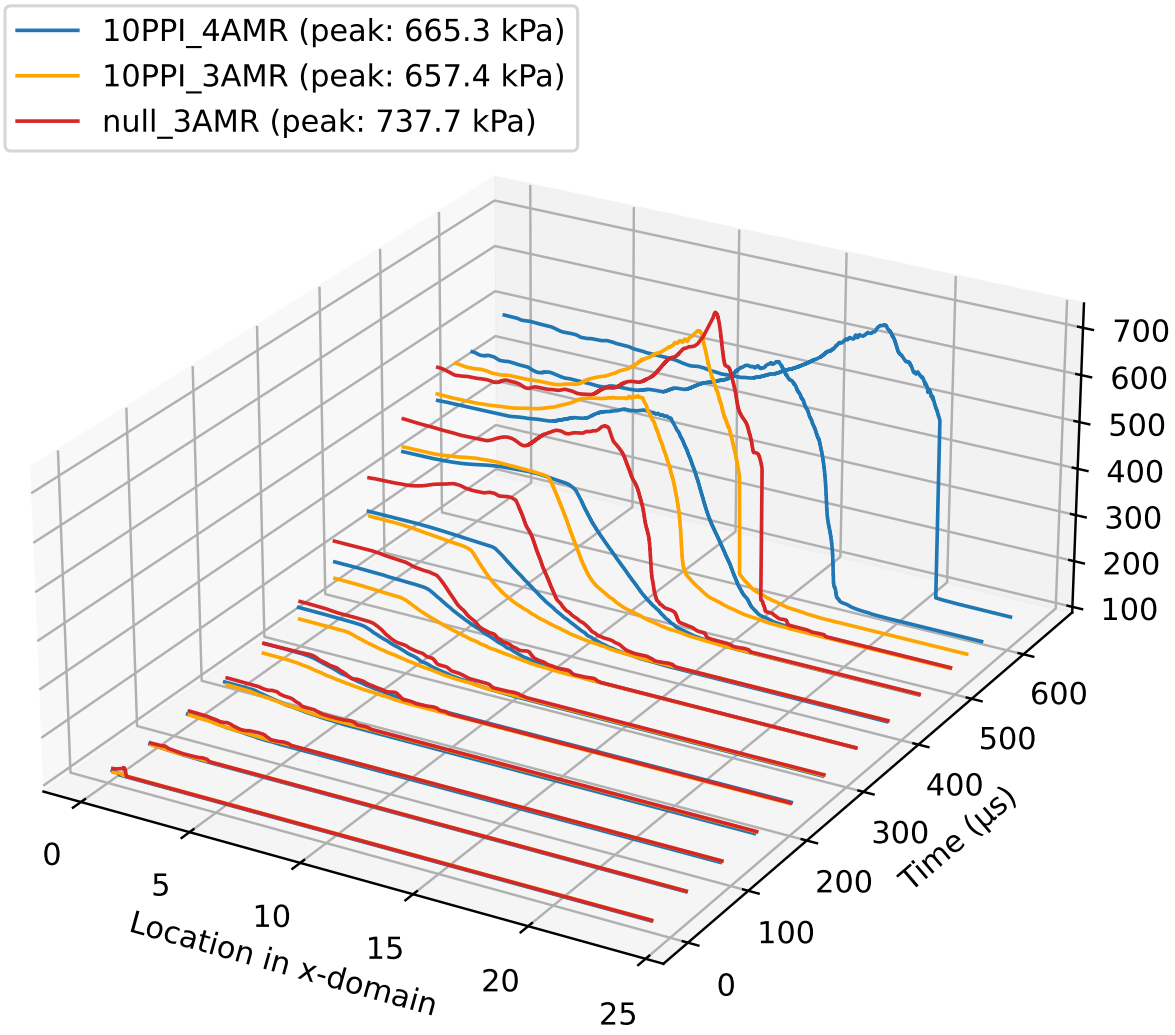

Figure 4.9: Row-averaged pressure profiles extracted from the tube centerline at representative times for the 10PPI 4AMR (blue), 10PPI 3AMR (orange) and Null 3AMR (red) simulations, measured in kPa

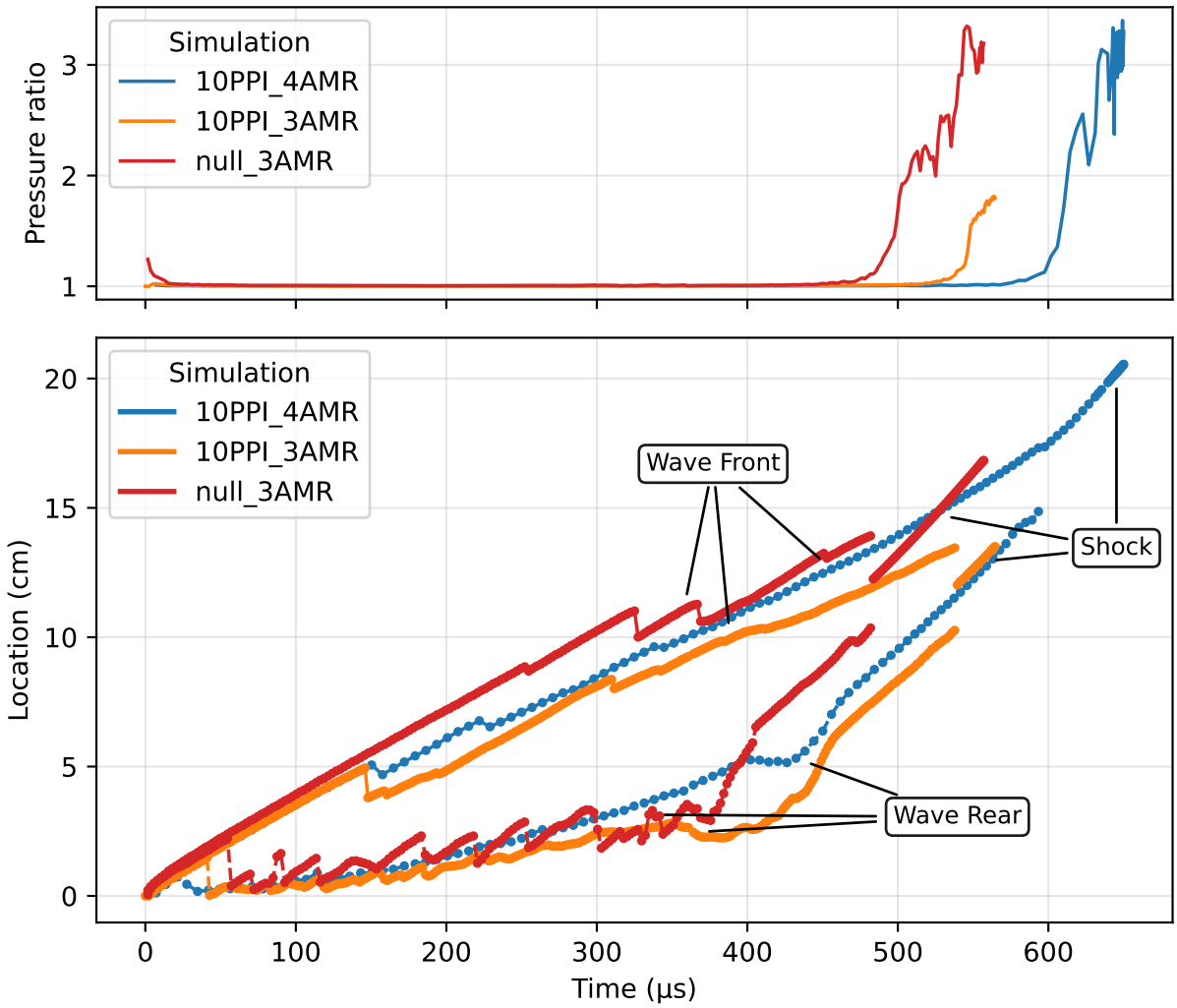

Figure 4.10: Comparison of the development of the leading shock. Pressure ratio (top) and shock components (bottom). Simulations are denoted as 10PPI 4AMR (blue), 10PPI 3AMR (orange) and Null 3AMR (red).

4.5 Notable Observations

This section is to present observations that are considered significant in the development of this work. There are three primary observations that are noted; a decrease in temperature in the core of the flame as it passes over the pores, a rippling of the pressure field in the presence of pores, and the development of a higher intensity pressure wave in the corners of the domain.

4.5.1 Temperature drop over pores

In the core of the domain the flame front curved back toward the wall. The core flame front was typically $2-3cm$ ahead of where the flame met the wall. As the flame in contact with the porous wall traversed the pores a temperature drop was observed. Figure 4.11 shows a smear plot as the flame traversing the porous surface. The pores are denoted in cyan on the edges of the domain and the region of interest is highlighted in green squares. It can seen that a region of decreased temperature extends into the core of the flame and persists behind the flame front. The dip in the temperature profile can be seen in Figure 4.12. From the neighbouring peaks to the trough it amounts to a drop of $\approx 40-50K$.

In Figure 4.13 the y-velocity in the same smear is presented. What can be observed is a region of strong negative y-velocity back into the core immediately after the flame front. This is to be expected as the flame takes a convex shape, the y-velocity is into the core directly behind the flame as the flow is expanding away from the peak pressure that comes along with the high temperature of the flame front. The flow is observed to quickly flip

direction after the flame passes and begin mass flow out of the pores, demonstrated by the positive y-velocity into the pore outlets. The observed pocket of reduced temperature that is transiting toward the core is flow caught in vortices at the boundary of the reversal of the flow direction. Indeed this aligns well with the decreased core and wall temperatures that are observed in the 10PPI 4AMR smear plot of Figure 4.6.

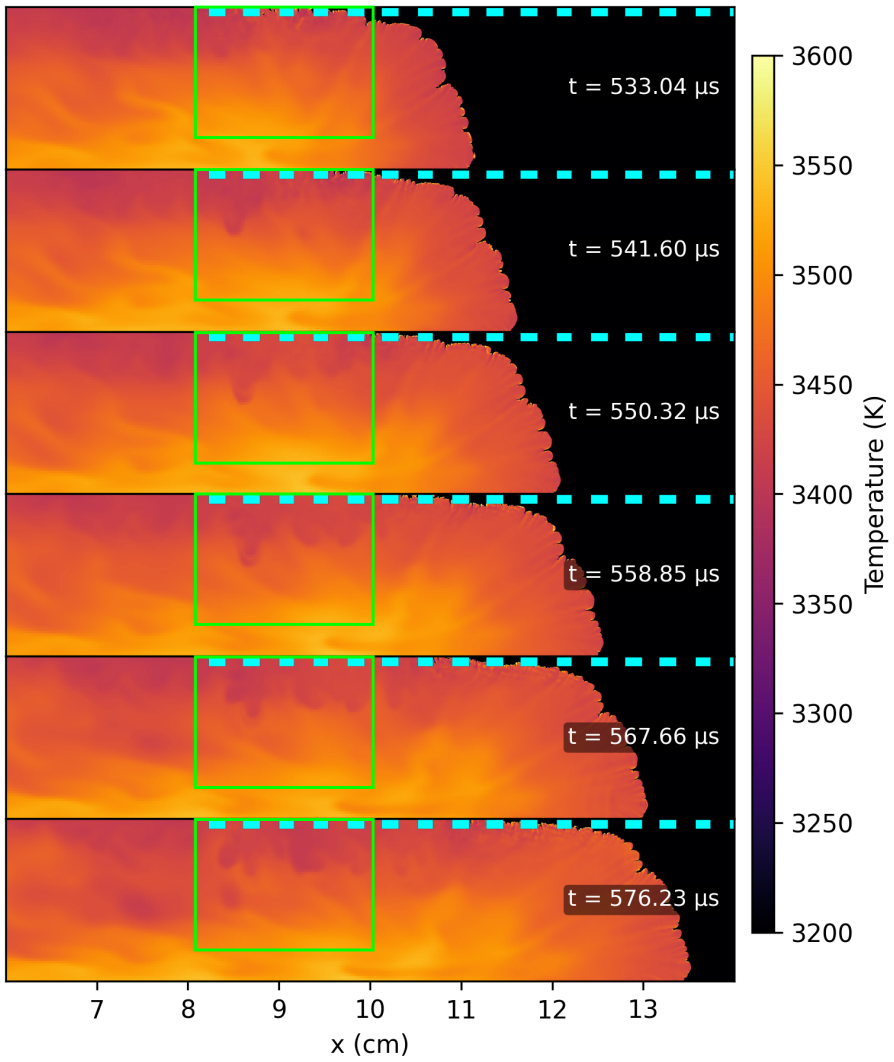

Figure 4.11: Smear plot of temperature decrease over pores (10PPI 4AMR)

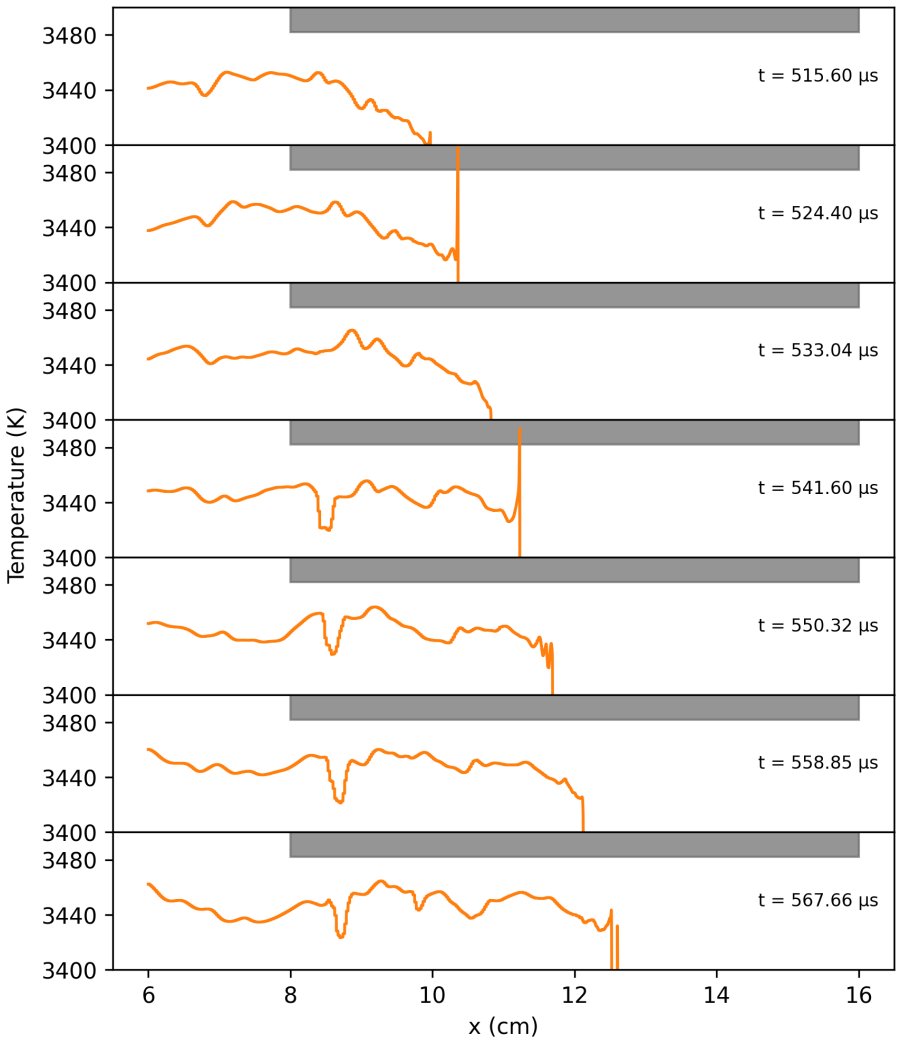

Figure 4.12: Smear plot of temperature decrease over pores (10PPI 4AMR), porous region denoted in grey. Temperature profile is taken at 65% toward wall to avoid wall noise. Specifically referring to the region denoted in green in Fig. 4.11.

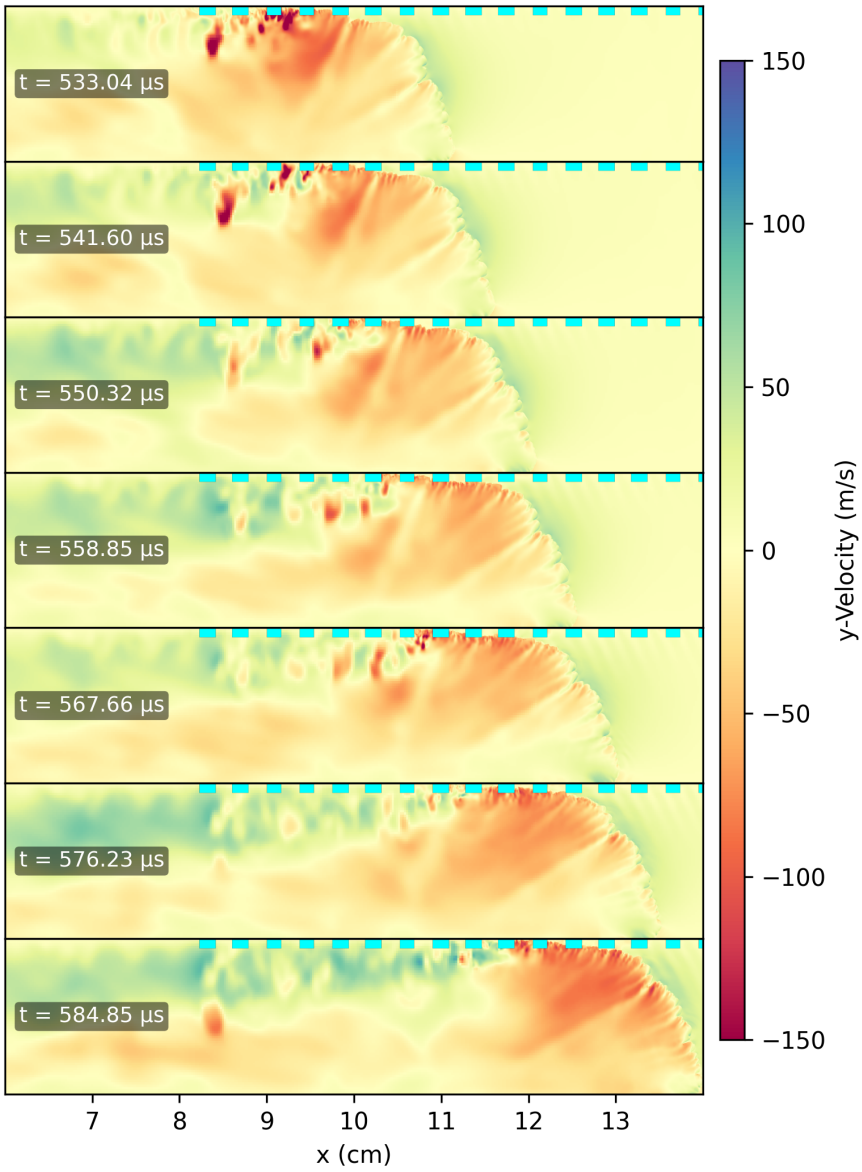

Figure 4.13: Smear plot of y-velocity profile in region of core temperature drop

4.5.2 Pressure ripples emanating from pores

Pressure perturbations, or "ripples", originate at the pore edges and extend approximately 45° into the core ahead of the flame. The perturbations themselves can be seen in image (a) of Figure 4.15. The amplitude of these perturbations increases as the flame progresses through the porous section. They are at their peak strength nearest to the flame front and they dissipate ahead of the flame as the overall pressure between the flame front and the diffuse region or shock front decreases. This is creating a concave pressure gradient ahead of the flame front that is driving flow toward the porous wall which can be seen in the y-velocity field, image (b) of Figure 4.15. The porous boundary alters the pressure field adjacent to the wall, allowing pressure driven flow to vent through the pores.

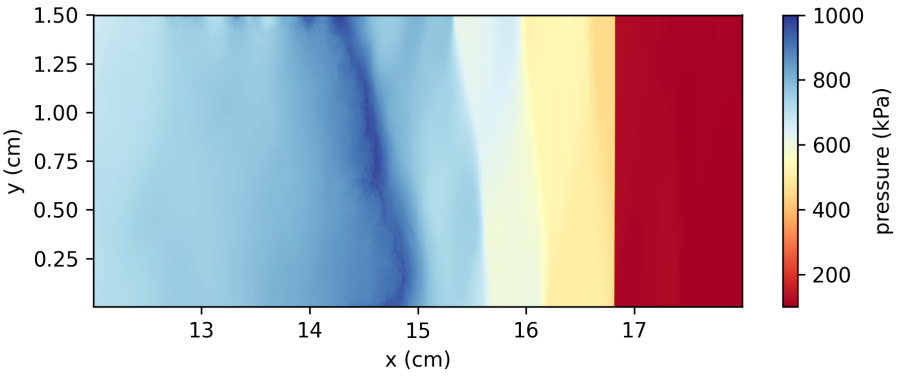

Figure 4.14: Developed pressure field of the Null 3AMR simulation

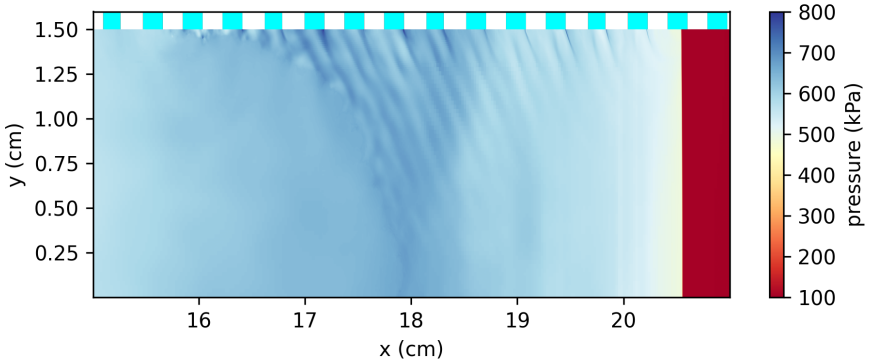

(a)

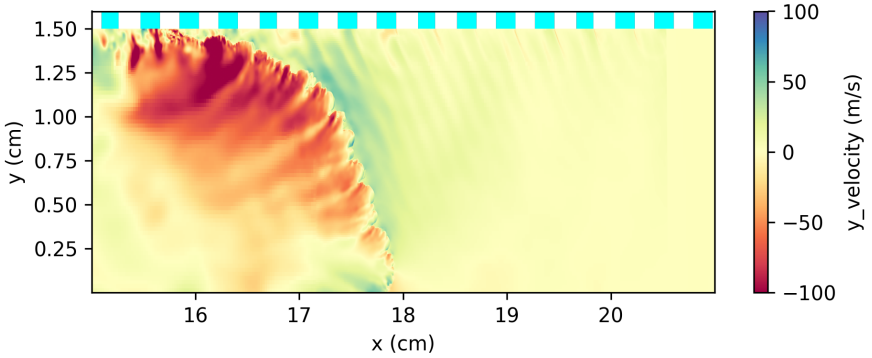

(b)

Figure 4.15: Pressure perturbations emanating from the pore edges, presented in (*a*) pressure and (*b*) y-velocity fields for the 10PPI 4AMR simulation

When compared to Figure 4.14 the layered build up of the pressure gradient is stronger and more compact even though it was developed over a shorter period of time. It also exhibits the convex shaping of the flame front, bending toward the wall and straightening as the gradient descends toward the developing shock front. It lacks the concave gradient seen in the pore case.

This observation is most significant in the corners of the domain near the wall where

the plain no-slip wall meets the porous wall. Here the flame has pulled back the most as the convex front presents in 3-dimensions. The pressure ripples extend through the much larger gap up to the shock front acting as described previously, to extract flow from the region ahead of the flame. In comparison the corners of the Null 3AMR simulation contain the highest pressure regions where the pressure fluctuations that reflect through the channel combine constructively to make the most significant jumps behind the shock front. This can be seen in Figure 4.16 which compares the development of the pressure field.

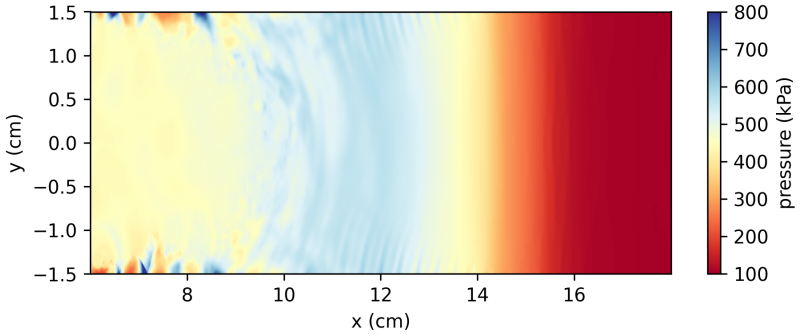

(a)

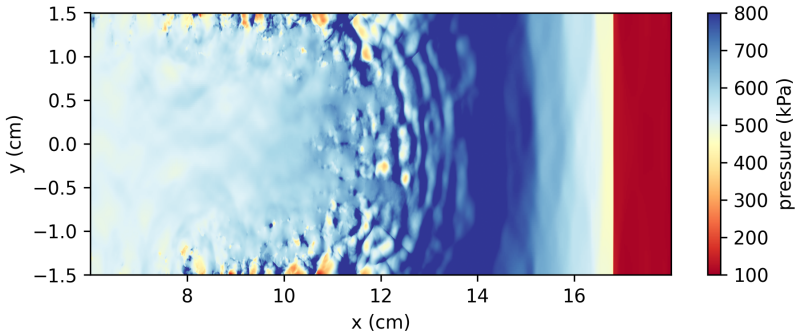

(b)

Figure 4.16: Comparison of pressure field near wall at t = $\approx 557.5\mu s$, (a) is the 10PPI 4AMR case, (b) is the Null 3AMR case

Chapter 5

Discussion

This chapter presents an interpretation of the results presented in Chapter 4 Results, with emphasis placed on the physical mechanisms governing the observed behaviour. The discussion is structured around four principal themes: flame acceleration, the higher flame speeds predicted by the simulations compared with the experimental observations of Jiang and Lin, the interpretation of the pressure field and its implications for acoustic energy loss, and the influence of the bulk flow field on the flow within the porous structure.

The hypotheses investigated in this work were motivated by the experimental observations of Jiang [41] and Lin [62]. Their experiments demonstrated that, following divergence of the flame into the porous copper foam, combustion within the porous structure accelerated before contributing to the subsequent acceleration of the bulk flame in the primary flow domain. This internal flame propagation was attributed to nozzle-like acceleration through the pore throats, followed by localized explosive events within the porous medium. They

further observed that detonation initiated adjacent to the porous wall rather than within the bulk flow and proposed that acoustic energy from the leading pressure wave was transferred into the porous medium, where repeated reflections increased the thermal energy of the porous structure prior to detonation initiation. Based on these observations, the present work hypothesized that flame divergence into the pores would promote flame acceleration through increased flame surface area and that interactions between the flame and pore surfaces would generate pressure gradients that promoted earlier shock development.

The flame speed results provide the first indication of the influence of the porous boundary condition on flame development. The simulations used the same ethylene-oxygen quiescent mixture and domain dimensions as the experiments of Jiang and Lin; however, the porous region was represented exclusively as an outlet boundary condition rather than as a resolved porous medium. Consequently, interactions occurring within the internal pore structure, including combustion within the pores and subsequent flow re-entry into the bulk domain, were not captured. Additionally, the simulations were ignited at the rear wall, whereas the experimental flame was initiated 3cm downstream along the side wall, resulting in reduced interaction between the simulated flame and the confining wall prior to reaching the porous region.

Comparison of the Null 3AMR and 10PPI 3AMR simulations indicates that the porous outlet boundary does not produce a measurable reduction in bulk flame velocity over the interval available for direct comparison. The two velocity profiles remain closely aligned from ignition to the termination of the 10PPI 3AMR simulation at a bulk flame position of approximately 11.7 cm, including approximately 3.7 cm of propagation beyond the beginning of the porous region at 8 cm. This result is significant because both simulations

employ the same maximum AMR level and differ principally in the wall boundary condition. The divergence previously observed between the Null 3AMR and 10PPI 4AMR simulations therefore cannot be attributed solely to the porous boundary. The 10PPI 4AMR flame begins to diverge from both 3AMR cases upstream of the porous region and subsequently maintains a lower flame velocity that is attributable to the grid sensitivity.

Despite the absence of a measurable reduction in flame velocity between the equal-resolution numerical cases, none of the simulations reproduce the flame-acceleration behaviour reported experimentally by Jiang and Lin. The numerical flames initially propagate substantially faster than the experimental flame, while the experimental flame subsequently undergoes a rapid acceleration after approximately 10 cm and exceeds the simulated velocities. In contrast, the Null 3AMR and 10PPI 3AMR simulations continue along similar acceleration trajectories over their common spatial interval. The absence of enhanced acceleration in the 10PPI 3AMR simulation indicates that representing the porous structure solely as an outlet boundary is insufficient to reproduce the experimentally observed acceleration associated with the porous medium. This supports the experimental observation that interactions between the pore body flame and the bulk domain flame serve to cause flame acceleration.

What is striking is how early the porous boundary begins influencing the developing pressure field ahead of the flame. Figure 4.9 shows the three-dimensional development of the row-averaged pressure profiles, with separation between the Null 3AMR and porous cases developing before the flame itself reaches the porous region. The equal-resolution comparison provides the clearest measure of this effect. At approximately 400 μs, the detected pressure ratios remain similar at 1.009 and 1.006 for the Null 3AMR and 10PPI

3AMR cases, respectively. By approximately 450 μs, these values have increased to 1.026 and 1.006, indicating the beginning of a measurable difference in pressure-wave amplification. The 10PPI 4AMR simulation exhibits the same qualitative behaviour, with a more gradual buildup of the pressure field than observed in the Null 3AMR case. The pressure field can therefore interact with the porous outlet boundary before arrival of the flame front, allowing pressure-driven flow through the pores without requiring direct flame-pore interaction.

This difference becomes pronounced during the subsequent development of the compression wave. At approximately 500 μs, the Null 3AMR simulation has reached a pressure ratio of 1.594, compared with only 1.017 in the 10PPI 3AMR simulation. Correspondingly, the Null 3AMR case satisfies the shock-detection criterion at approximately 483.6 μs and 12.25 cm, whereas the 10PPI 3AMR case satisfies the same criterion at approximately 539.5 μs and 12.02 cm. The porous boundary therefore delays shock formation by approximately 56 μs while producing little change in the axial location of shock formation at equal resolution. The higher-resolution 10PPI 4AMR simulation similarly exhibits delayed pressure-wave steepening and reaches a peak row-averaged pressure of approximately 665 kPa, closely matching the 657 kPa peak of the 10PPI 3AMR case, while the Null 3AMR simulation reaches approximately 738 kPa. The peak pressures of the two porous simulations differ by only approximately 1.2%, while remaining approximately 10-11% below the Null 3AMR peak. The agreement in peak pressure between the two porous simulations, despite their different refinement levels, supports the conclusion that the attenuation of the developing pressure field is associated with the porous outlet boundary rather than solely with grid resolution.

Jiang [41] and Lin [62] proposed that acoustic energy associated with the developing shock was transferred into the porous medium. The present results suggest that interaction with the porous boundary begins prior to the formation of a distinct shock front. Energy is extracted continuously from the developing pressure field, delaying the formation of a mature shock rather than merely weakening an existing one. This behaviour is most clearly demonstrated by the equal-resolution comparison in Figure 4.10. The Null 3AMR simulation first satisfies the shock-detection criterion at approximately 483.6 μs and an axial location of 12.25 cm, whereas the 10PPI 3AMR simulation satisfies the same criterion at approximately 539.5 μs and 12.02 cm. Relative to the Null 3AMR case, this corresponds to an approximately 11.6% increase in shock-formation time, while the axial formation location differs by only approximately 1.9%. The substantially larger temporal difference indicates that the primary influence of the porous boundary is on the rate of pressure-wave buildup rather than the distance required for shock formation. The 10PPI 4AMR simulation exhibits a further temporal and spatial delay in shock development, indicating that the precise shock-formation time and location remain sensitive to grid refinement. Nevertheless, both porous simulations exhibit delayed pressure-wave steepening relative to the Null 3AMR case.

To quantify the transport associated with this pressure-field interaction, mass and kinetic-energy fluxes were evaluated across a plane located immediately below the porous boundary. The net mass flux remained small during the early stages of flame propagation, but increased rapidly as the flame and associated high-pressure products approached and entered the porous region. By the end of the 10PPI 4AMR simulation, approximately 3.6 mg of net mass had been transported outward across this plane. The cumulative out-

ward kinetic-energy transport exhibited a similar temporal behaviour, remaining negligible during early flame propagation before increasing rapidly after approximately 450-500 μs, ultimately reaching approximately 0.22 J. This net mass represents 1.3% of the total initialized system mass as having exited through the pores. As these quantities were evaluated on a near-wall control plane rather than directly at the computational boundary, they represent transport toward the porous outlets rather than exact boundary-integrated losses. Nevertheless, the results quantitatively demonstrate that the development of the pressure field is accompanied by increasing outward transport through the porous region, with the strongest extraction occurring following the arrival of the flame and high-pressure products.

The y-velocity field presented in Figure 4.13 provides further insight into the local flow responsible for this transport and into the interaction between the bulk flame and porous structure. Jiang [41] and Lin [62] observed that combustion within the porous structure accelerated more rapidly than the bulk flame during portions of the propagation process, but did not continue to propagate independently ahead of the bulk flame. Instead, the two regions remained coupled as the overall flame accelerated. The present simulations suggest a flow mechanism through which such coupling may occur.

As the flame propagates along the porous boundary, the bulk flame develops a convex structure associated with the asymmetric interaction between the reacting flow and the wall. Ahead of and during passage of the flame, the transverse velocity field exhibits motion away from the porous surface and toward the core of the reacting region. Following passage of the flame front, the local flow direction reverses, producing motion back toward the porous boundary. The mass-flux analysis supports this observation: although net

transport across the near-wall control plane remains outward, appreciable inward-directed transport develops after approximately 500 μs, coincident with the period of strongest interaction between the reacting flow and porous region. The simultaneous presence of outward and inward-directed transport therefore indicates that the near-wall flow is not characterized by simple unidirectional venting, but by a dynamically coupled exchange superimposed on a net outward mass flux.

Although combustion within the pore volume is not resolved in the present simulations, this flow behaviour provides a potential mechanism for the acceleration observed experimentally by Jiang and Lin. Flow directed away from the porous surface may allow disturbances generated near the porous structure to influence the bulk reacting region, while subsequent flow directed toward the surface provides a mechanism for the bulk flow to interact with combustion occurring within the porous structure. In the experiments, where the pores contain a reacting mixture rather than functioning solely as outlets, this bidirectional coupling could permit combustion within the porous structure and the bulk flame to evolve as a coupled system. The present surface-only representation cannot reproduce this internal combustion process, which may explain why the rapid flame acceleration observed experimentally is absent from the simulations.

Overall, the present results indicate that the influence of a porous boundary on DDT is governed by competing and interacting mechanisms. The porous outlets alter the development of the pressure field through continuous mass and energy transport, producing delayed pressure-wave steepening and shock formation. However, the equal-resolution comparison between the Null 3AMR and 10PPI 3AMR simulations demonstrates that this pressure attenuation does not produce a measurable reduction in bulk flame velocity over the available

simulation interval. At the same time, the transverse velocity field demonstrates a dynamically coupled near-wall flow, with both outward and inward-directed transport occurring during interaction of the flame with the porous region. The surface-only porous representation therefore captures pressure attenuation and aspects of the flow coupling, but cannot reproduce combustion and transport within the porous volume itself. These unresolved internal processes appear necessary to explain the rapid flame acceleration observed experimentally by Jiang and Lin. Future simulations incorporating resolved porous geometry will be required to determine how internal combustion, flow exchange, and pressure-wave interactions combine to produce the experimentally observed acceleration and detonation initiation behaviour.

Chapter 6

Conclusion

The work conducted herein investigated the influence of porous boundary interactions on flame acceleration and shock development during deflagration-to-detonation transition (DDT). The study was motivated by the experimental investigations of Jiang [41] and Lin [62], who demonstrated successful transition from a slowly propagating deflagrative flame to a supersonic detonative flame within a 30 mm $\times$ 30 mm square channel containing copper foam porous media along the channel walls. In their experiments, combustion within the porous structure contributed to acceleration of the bulk flame and subsequent detonation initiation.

The present work investigated these observations numerically using a stoichiometric ethylene-oxygen mixture within an equivalent domain. Null and porous configurations were simulated, with the copper foam represented using a custom boundary condition consisting of evenly spaced circular pores acting as outlets. This approach isolated the

influence of surface-level mass transport through the porous boundary while excluding combustion and transport within the internal pore structure. Simulations at multiple levels of adaptive mesh refinement were additionally used to assess the sensitivity of the observed behaviour to grid resolution.

Based on the observations of Jiang and Lin, it was hypothesized that interaction with the porous structure would increase flame acceleration through additional flame surface area and stretching effects, while pressure gradients generated around the pore openings would contribute to development of the leading shock wave. The present results did not reproduce the experimentally observed enhancement in flame acceleration. In the equal-resolution comparison, the Null 3AMR and 10PPI 3AMR simulations exhibited similar bulk flame velocities over the available simulation interval, including after the flame entered the porous region. The reduced flame velocity observed in the 10PPI 4AMR simulation therefore could not be attributed solely to the porous boundary and demonstrated that the predicted flame acceleration remained sensitive to grid refinement.

Despite the absence of a measurable influence on bulk flame velocity at equal resolution, the porous boundary produced a clear influence on pressure-wave development. The Null 3AMR simulation satisfied the shock-detection criterion at approximately 483.6 μs and 12.25 cm, compared with approximately 539.5 μs and 12.02 cm for the 10PPI 3AMR simulation. The approximately 11.6% increase in shock-formation time, accompanied by only an approximately 1.9% difference in axial formation location, indicates that the porous boundary primarily influenced the rate of pressure-wave buildup rather than the distance required for shock formation. Interaction between the developing pressure field and porous boundary was observed prior to arrival of the flame at the porous region, indicating that

pressure and flow interactions with the outlets begin before direct flame-pore interaction.

Mass and kinetic-energy transport through a near-wall control plane further quantified this interaction. In the 10PPI 4AMR simulation, net outward mass transport increased rapidly as the flame and high-pressure products interacted with the porous region, reaching approximately 3.6 mg cumulatively by the end of the simulation. Cumulative outward kinetic-energy transport across the same plane reached approximately 0.22 J. Although these control-plane quantities do not represent direct measurements of the computational boundary flux, they demonstrate that the altered pressure-wave development is accompanied by increasing outward mass and kinetic-energy transport toward the porous outlets.

A further observation from the transverse velocity field was the reversal of near-wall flow during flame propagation along the porous boundary. Flow directed away from the porous surface during flame passage was followed by inward-directed motion toward the porous region, while the net transport across the near-wall control plane remained outward. This behaviour demonstrates that the near-wall interaction is not characterized solely by unidirectional venting, but contains a dynamically coupled exchange between the bulk flow and porous boundary. Although the strength of this coupling cannot be quantified directly from the present surface-only simulations, it provides a potential mechanism through which combustion within a resolved porous structure could interact with the bulk flame, consistent with the coupled acceleration observed experimentally by Jiang and Lin.

Overall, the present results demonstrate that an outlet-only porous boundary is insufficient to reproduce the flame-acceleration and detonation-initiation behaviour observed experimentally. The surface representation captures mass and kinetic-energy transport

through the porous boundary, pressure-wave attenuation, delayed shock development, and near-wall flow coupling, but does not resolve combustion and transport within the porous volume. These internal processes appear necessary to reproduce the rapid acceleration observed experimentally. Future numerical investigations should therefore incorporate resolved porous geometries capable of capturing internal combustion, transport through pore throats, and feedback between the porous and bulk reacting regions. Such simulations would enable the relative contributions of pressure-field attenuation and pore-scale combustion-driven flow coupling to DDT to be determined.

References

[1] The world's first space flight for the rotating detonation engine, and a glimpse at a new sample return capsule — cosmos.isas.jaxa.jp. https://cosmos.isas.jaxa.jp/the-worlds-first-space-flight-for-the-rotating-detonation-engine-and-a-glimpse-at 2022. [Accessed 09-04-2026].

[2] Jacqueline. Akhavan. *The chemistry of explosives*. Royal Society of Chemistry, Cambridge, UK, 3rd ed. edition, 2011.

[3] VS Babkin and LS Kozachenko. Development of detonation in gases in rough tubes. *Zh. Prikl. Mekh. Tekh. Fiz*, (3):165–174, 1960.

[4] Larine Barr. Pulsed detonation engine flies into history. https://www.af.mil/News/Article-Display/Article/123534/pulsed-detonation-engine-flies-into-history/, 2008. [Accessed 09-04-2026].

[5] Clinton Bedick, Don Ferguson, and Peter Strakey. Characterization of rotating detonation engine injector response using laser-induced fluorescence. *Journal of Propul-*

sion and Power, 35(4):827–838, 2019.

[6] G Yu Bivol, SV Golovastov, and VV Golub. Detonation suppression in hydrogen–air mixtures using porous coatings on the walls. *Shock Waves*, 28(5):1011–1018, 2018.

[7] G Yu Bivol, SV Golovastov, and VV Golub. Investigation of hydrogen-air and acetylene-air flame propagation through porous media using infrared visualisation. *Process Safety and Environmental Protection*, 163:368–383, 2022.

[8] Grigory Bivol and Sergey Golovastov. Effects of polyurethane foam on the detonation propagation in stoichiometric hydrogen-air mixture. *Process Safety and Environmental Protection*, 130:14–21, 2019.

[9] AA Borisov. On the origin of exothermic centers in gaseous mixtures. *Acta Astronautica*, 1(7-8):909–920, 1974.

[10] Meherwan P Boyce. *Gas turbine engineering handbook*. Elsevier, 2011.

[11] Derek Bradley. Autoignitions and detonations in engines and ducts. *Philosophical Transactions: Mathematical, Physical and Engineering Sciences*, pages 689–714, 2012.

[12] CK Chan, WA Dewit, and GW Koroll. Criteria for transition from deflagration to detonation in h 2-air-steam mixtures. In *Heat and Mass Transfer in Severe Nuclear Reactor Accidents. Proceedings of the International Symposium*. Begel House Inc., 1995.

[13] David Leonard Chapman. Vi. on the rate of explosion in gases. *The London, Edinburgh, and Dublin Philosophical Magazine and Journal of Science*, 47(284):90–104, 1899.

[14] William Ronald Chapman and Richard Vernon Wheeler. Cclxxxiii.—the propagation of flame in mixtures of methane and air. part iv. the effect of restrictions in the path of the flame. *Journal of the Chemical Society (Resumed)*, 129:2139–2147, 1926.

[15] RS Chue, JF Clarke, and JH Lee. Chapman-jouguet deflagrations. *Proceedings of the Royal Society of London. Series A: Mathematical and Physical Sciences*, 441(1913):607–623, 1993.

[16] G Ciccarelli, C Johansen, and M Parravani. Transition in the propagation mechanism during flame acceleration in porous media. *Proceedings of the Combustion Institute*, 33(2):2273–2278, 2011.

[17] Gaby Ciccarelli, Craig T Johansen, and Michael Parravani. The role of shock–flame interactions on flame acceleration in an obstacle laden channel. *Combustion and flame*, 157(11):2125–2136, 2010.

[18] Jackson Crane, Jonathan T Lipkowicz, Xian Shi, Irenaeus Wlokas, Andreas M Kempf, and Hai Wang. Three-dimensional detonation structure and its response to confinement. *Proceedings of the combustion institute*, 39(3):2915–2923, 2023.

[19] Jackson Crane, Xian Shi, Jonathan T Lipkowicz, Andreas M Kempf, and Hai Wang. Geometric modeling and analysis of detonation cellular stability. *Proceedings of the combustion institute*, 38(3):3585–3593, 2021.

[20] L Crussard. Ondes de choc et onde explosive. *Bull. Soc. Industr. Min. St-Etienne, Ser. 4*, 6:257–364, 1907.

[21] Pinku Debnath and Krishna Murari Pandey. Computational fluid dynamics simulation of detonation wave propagation in modified pulse detonation combustor. In *E3S Web of Conferences*, volume 430, page 01243. EDP Sciences, 2023.

[22] Jan C Deeken, DI Suslov, Michael Oschwald, Stefan Schlechtriem, and OJ Haidn. Propellant atomization for porous injectors. *Journal of Propulsion and Power*, 35(6):1116–1126, 2019.

[23] Digital Research Alliance of Canada. Advanced research computing and data management services. https://alliancecan.ca, 2026. Accessed: 2026-07-08.

[24] Sergey B Dorofeev. Hydrogen flames in tubes: critical run-up distances. *International journal of hydrogen energy*, 34(14):5832–5837, 2009.

[25] Quentin Douasbin. *Acoustic waves in combustion devices: interactions with flames and boundary conditions*. PhD thesis, Institut National Polytechnique de Toulouse-INPT, 2018.

[26] Chris A Eckett, James J Quirk, and Joseph E Shepherd. The role of unsteadiness in direct initiation of gaseous detonations. *Journal of Fluid Mechanics*, 421:147–183, 2000.

[27] Marjorie W Evans, Frank I Given, and William E Richeson Jr. Effects of attenuating materials on detonation induction distances in gases. *Journal of Applied Physics*, 26(9):1111–1113, 1955.

[28] Wildon Fickett and William C Davis. Detonation: theory and experiment. 2012.

[29] Vadim N Gamezo, Daniel Desbordes, and Elaine S Oran. Formation and evolution of two-dimensional cellular detonations. *Combustion and Flame*, 116(1-2):154–165, 1999.

[30] Vadim N Gamezo, Takanobu Ogawa, and Elaine S Oran. Numerical simulations of flame propagation and ddt in obstructed channels filled with hydrogen–air mixture. *Proceedings of the Combustion Institute*, 31(2):2463–2471, 2007.

[31] Irvin Glassman, Richard A. Yetter, and Nick G. Glumac. Chapter 5 - detonation. In *Combustion (Fifth Edition)*, pages 255–299. Academic Press, Boston, fifth edition edition, 2015.

[32] K Goto, R Yokoo, A Kawasaki, K Matsuoka, J Kasahara, A Matsuo, I Funaki, and H Kawashima. Investigation into the effective injector area of a rotating detonation engine with impact of backflow. *Shock Waves*, 31(7):753–762, 2021.

[33] Changming Guo, Geraint Thomas, Jian Li, and Deliang Zhang. Experimental study of gaseous detonation propagation over acoustically absorbing walls. *Shock waves*, 11(5):353–359, 2002.

[34] Wenhu Han, Yang Gao, and Chung K Law. Flame acceleration and deflagration-to-detonation transition in micro-and macro-channels: An integrated mechanistic study. *Combustion and Flame*, 176:285–298, 2017.

[35] Josef Haßlberger. *Numerical simulation of deflagration-to-detonation transition on industry scale*. PhD thesis, Technische Universität München, 2017.

[36] Jiahui He, Jianling Li, Xiao Ma, Baoqing Meng, and Baolin Tian. Reduction and applicability of chemical kinetic model for ethylene detonation simulation. *Fuel*, 342:127812, 2023.

[37] A Heidari and Jennifer X Wen. Flame acceleration and transition from deflagration to detonation in hydrogen explosions. *International journal of hydrogen energy*, 39(11):6184–6200, 2014.

[38] H Hugoniot. Mémoire sur la propagation du mouvement dans un fluide indéfini (première partie). *Journal de Mathématiques Pures et Appliquées*, 3:477–492, 1887.

[39] J. D. Hunter. Matplotlib: A 2d graphics environment. *Computing in Science & Engineering*, 9(3):90–95, 2007.

[40] Sigmund J Jacobs. The energy of detonation. Technical report, 1956.

[41] Yuguang Jiang, Yong Lin, Qi Wang, Xiaojia Fang, Xudong Jiang, and Wei Fan. Effects of porous wall on deflagration to detonation transition and detonation wave propagation. *Physics of Fluids*, 36(9), 2024.

[42] Zeren Jiao, Harold U Escobar-Hernandez, Trent Parker, and Qingsheng Wang. Review of recent developments of quantitative structure-property relationship models on fire and explosion-related properties. *Process Safety and Environmental Protection*, 129:280–290, 2019.

[43] Craig Johansen and Gaby Ciccarelli. Combustion in a horizontal channel partially filled with a porous media. *Shock Waves*, 18(2):97–106, 2008.

[44] Craig T Johansen and Gaby Ciccarelli. Visualization of the unburned gas flow field ahead of an accelerating flame in an obstructed square channel. *Combustion and Flame*, 156(2):405–416, 2009.

[45] Emile Jouguet. Sur la propagation des réactions chimiques dans les gaz. *J. Maths. Pure Appl.*, 7:347, 1905.

[46] Aditya Karanam, Vishnu Verma, and Jayanta Chattopadhyay. Numerical modelling of deflagration to detonation transition in hydrogen air mixtures. 2021.

[47] Karlsruhe Institute of Technology. Runtime record and first electricity generation with a compressorless hydrogen gas turbine. Press Release 010/2026, 02 2026.

[48] Alexei Kotchourko and Thomas Jordan. *Hydrogen Safety for Energy Applications: Engineering Design, Risk Assessment, and Codes and Standards*. Butterworth-Heinemann, 2022.

[49] Yutaro Koyama, Naotaro Suto, Ken Matsuoka, Noboru Itouyama, Jiro Kasahara, Masaaki Yasui, Yuichiro Ide, Japan Akira Kawasaki, Shizuoka Hamamatsu, and Japan Hiroaki Watanabe. Design of a premixed rotating detonation engine with a porous injector.

[50] Allen L Kuhl, Antoni Koichi Hayashi, and Piotr Wolański. The contribution of ak oppenheim to explaining the nature of the initiation of gaseous detonation in tubes. *Transactions on Aerospace Research*, 2022(2), 2022.

[51] P Laffitte. Sur la propagation de l'onde explosive. *CR Acad. Sci., Paris*, 177:178–180, 1923.

[52] Paul Laffitte. Recherches expérimentales sur l'onde explosive et l'onde de choc. In *Annales de Physique*, volume 10, pages 587–694. EDP Sciences, 1925.

[53] John HS Lee. Initiation of gaseous detonation. *Annual Review of Physical Chemistry*, 28(1):75–104, 1977.

[54] John HS Lee. Dynamic parameters of gaseous detonations. *Annual review of fluid mechanics*, 16:311–336, 1984.

[55] John HS Lee. The propagation of turbulent flames and detonations in tubes. In *Advances in chemical reaction dynamics*, pages 345–378. Springer, 1986.

[56] John HS Lee. *The detonation phenomenon*. Cambridge University Press, 2008.

[57] John HS Lee, R Knystautas, and A Freiman. High speed turbulent deflagrations and transition to detonation in h2 air mixtures. *Combustion and flame*, 56(2):227–239, 1984.

[58] Jian-Ling Li, Wei Fan, Chuan-Jun Yan, Hong-Yan Tu, and Kai-Cheng Xie. Performance enhancement of a pulse detonation rocket engine. *Proceedings of the Combustion Institute*, 33(2):2243–2254, 2011.

[59] Yuntao Li, Sheng Qi, Qi Jing, Laibin Zhang, Dan Wang, Congling Shi, Houjia Xu, Yueyang Li, Zelin Wu, and Rui Zhou. The effect of operating frequency and ignition energy on jp-10/po/aluminum powder multiphase-pulse-detonation-engine. *Applied Thermal Engineering*, 244:122758, 2024.

[60] Yuntao Li, Sheng Qi, Qi Jing, Laibin Zhang, Dan Wang, Congling Shi, Houjia Xu, Yueyang Li, Zelin Wu, and Rui Zhou. The effect of operating frequency and ignition energy on jp-10/po/aluminum powder multiphase-pulse-detonation-engine. *Applied Thermal Engineering*, 244:122758, 2024.

[61] MA Liberman, AD Kiverin, and MF Ivanov. On detonation initiation by a temperature gradient for a detailed chemical reaction models. *Physics Letters A*, 375(17):1803–1808, 2011.

[62] Yong Lin, Yuguang Jiang, Yang Luo, Shuhang Zhang, Qi Wang, and Wei Fan. Flame acceleration and detonation initiation process over porous flat wall. *Acta Astronautica*, 2025.

[63] Yunfeng Liu, Xin Han, and Zijian Zhang. Study on the propulsive performance of oblique detonation engine. *Energy*, 292:130519, 2024.

[64] Zhaorong Liu, Xiaoxi Li, Min Li, and Huahua Xiao. Flame acceleration and ddt in a channel with fence-type obstacles: Effect of obstacle shape and arrangement. *Proceedings of the Combustion Institute*, 39(3):2787–2796, 2023.

[65] Yasser Mahmoudi, Kiumars Mazaheri, and Saeed Parvar. Hydrodynamic instabilities and transverse waves in propagation mechanism of gaseous detonations. *Acta Astronautica*, 91:263–282, 2013.

[66] E Mallard and HL Le Chatelier. Thermal model for flame propagation. *Ann. Mines*, 4(18):379–568, 1883.

[67] M Marshall and JC Oxley. Explosives: the threats and the materials. In *Aspects of explosives detection*, page 12. Elsevier, 2009.

[68] Brian Maxwell, Andrzej Pekalski, and Matei Radulescu. Modelling of the transition of a turbulent shock-flame complex to detonation using the linear eddy model. *Combustion and Flame*, 192:340–357, 2018.

[69] Brian McNeilly Maxwell. *Turbulent combustion modelling of fast-flames and detonations using compressible LEM-LES*. PhD thesis, Université d'Ottawa/University of Ottawa, 2016.

[70] Kiumars Mazaheri, Yasser Mahmoudi, and Matei I Radulescu. Diffusion and hydrodynamic instabilities in gaseous detonations. *Combustion and Flame*, 159(6):2138–2154, 2012.

[71] John Michael McAfee. *The Deflagration-to-Detonation Transition*, pages 483–535. Springer Berlin Heidelberg, Berlin, Heidelberg, 2010.

[72] Cristian Mejía-Botero, Florent Virot, LF Figueira da Silva, and Josué Melguizo-Gavilanes. A detonation run-up distance database: data-driven existing models improvement and new model development. *Proceedings of the Combustion Institute*, 40(1-4):105444, 2024.

[73] AG Merzhanov. On critical conditions for thermal explosion of a hot spot. *Combustion and Flame*, 10(4):341–348, 1966.

[74] JW Meyer and AK Oppenheim. Coherence theory of the strong ignition limit. *Combustion and Flame*, 17(1):65–68, 1971.

[75] Hoi Dick Ng and John HS Lee. Direct initiation of detonation with a multi-step reaction scheme. *Journal of Fluid Mechanics*, 476:179–211, 2003.

[76] James Arthur Nicholls, HR Wilkinson, and Richard Boyd Morrison. Intermittent detonation as a thrust-producing mechanism. *Journal of jet propulsion*, 27(5):534–541, 1957.

[77] Antoni Kazimierz Oppenheim and Rem Ivanovich Soloukhin. Experiments in gasdynamics of explosions. *Annual Review of Fluid Mechanics*, 5(1):31–58, 1973.

[78] Elaine S Oran and Vadim N Gamezo. Origins of the deflagration-to-detonation transition in gas-phase combustion. *Combustion and flame*, 148(1-2):4–47, 2007.

[79] O Peraldi, R Knystautas, and JH Lee. Criteria for transition to detonation in tubes. In *Symposium (International) on Combustion*, volume 21, pages 1629–1637. Elsevier, 1988.

[80] JM Picone, ES Oran, JP Boris, and TR Young. Dynamics of shock waves, explosions, and detonations. *Prog Astro Aero*, 94:429–448, 1984.

[81] Aleksandr Vladimirovich Pinaev. Combustion modes and flame propagation criteria for an encumbered space. *Combustion, Explosion and Shock Waves*, 30(4):454–461, 1994.

[82] AA Putnam, FE Belles, and JAC Kentfield. Pulse combustion. *Progress in energy and combustion science*, 12(1):43–79, 1986.

[83] Xu Qin, Qingchun Yang, Hongxin Wang, Xu Xu, and Oskar Haidn. Research progress in rotating detonation propulsion technology. *Acta Astronautica*, 2025.

[84] Suryanarayan Ramachandran, Navneeth Srinivasan, Zhiyan Wang, Arsam Behkish, and Suo Yang. A numerical investigation of deflagration propagation and transition to detonation in a microchannel with detailed chemistry: Effects of thermal boundary conditions and vitiation. *Physics of Fluids*, 35(7), 2023.

[85] Venkat Raman, Supraj Prakash, and Mirko Gamba. Nonidealities in rotating detonation engines. *Annual Review of Fluid Mechanics*, 55(1):639–674, 2023.

[86] William John Macquorn Rankine. Xv. on the thermodynamic theory of waves of finite longitudinal disturbance. *Philosophical Transactions of the Royal Society of London*, (160):277–288, 1870.

[87] PM Rubins and THM Cunningham. Shock-induced supersonic combustion in a constant-area duct. *Journal of Spacecraft and Rockets*, 2(2):199–205, 1965.

[88] PM Rubins and RP Rhodes Jr. Shock-induced combustion with oblique shocks-comparison of experiment and kinetic calculations. *AIAA Journal*, 1(12):2778–2784, 1963.

[89] Hale J Sabine. The absorption of noise in ventilating ducts. *The Journal of the Acoustical Society of America*, 12(1):53–57, 1940.

[90] KS Sagar and Ramesh K Agarwal. Assessment of the wray-agarwal turbulence model for detonation combustion. In *AIAA SCITECH 2026 Forum*, page 2420, 2026.

[91] E Schmidt, H Steinicke, and U Neubert. Flame and schlieren photographs of the combustion of gas-air mixtures in tubes. *VDI-Forsch Ungsheft*, 431, 1951.

[92] KI Shchelkin. Influence of tube roughness on the formation and detonation propagation in gas. *J. Exp. Theor. Phys*, 10(10):823–82, 1940.

[93] Joseph E Shepherd. Detonation in gases. *Proceedings of the Combustion Institute*, 32(1):83–98, 2009.

[94] Joseph E Shepherd and J Kasahara. Analytical models for the thrust of a rotating detonation engine. *GALCIT Report FM2017*, 1, 2017.

[95] Joseph E Shepherd and John HS Lee. On the transition from deflagration to detonation. In *Major research topics in combustion*, pages 439–487. Springer, 1992.

[96] M Silvestrini, B Genova, G Parisi, and FJ Leon Trujillo. Flame acceleration and ddt run-up distance for smooth and obstacles filled tubes. *Journal of Loss Prevention in the Process Industries*, 21(5):555–562, 2008.

[97] Hariswaran Sitaraman, Shashank Yellapantula, Marc T. Henry de Frahan, Bruce Perry, Jon Rood, Ray Grout, and Marc Day. Adaptive mesh based combustion simulations of direct fuel injection effects in a supersonic cavity flame-holder. *Combustion and Flame*, 232:111531, 2021.

[98] Antoine Stock and Vincent Moureau. Feature-based adaptive mesh refinement for multi-regime reactive flows. *Proceedings of the Combustion Institute*, 40(1-4):105488, 2024.

[99] Tianyu Sun, Qibin Zhang, Liangxiao Chen, Ke Wang, and Wei Fan. Prediction of detonation initiation in an air-breathing pulse detonation combustor utilizing a simplified ethylene-air reaction mechanism. *Aerospace Science and Technology*, 129:107821, 2022.

[100] Craig M Tarver. Condensed matter detonation: theory and practice. In *Shock Waves Science and Technology Library, Vol. 6: Detonation Dynamics*, pages 339–372. Springer, 2011.

[101] M. J. Turk, B. D. Smith, J. S. Oishi, S. Skory, S. W. Skillman, T. Abel, and M. L. Norman. yt: A Multi-code Analysis Toolkit for Astrophysical Simulation Data. *The Astrophysical Journal Supplement Series*, 192:9, 2011.

[102] PA Urtiew and AK Oppenheim. Experimental observations of the transition to detonation in an explosive gas. *Proceedings of the Royal Society of London. Series A. Mathematical and Physical Sciences*, 295(1440):13–28, 1966.

[103] Venus Aerospace. World's first high-thrust rdre flight, 2025. Accessed on 11.05.2026.

[104] H Gg Wagner. Some experiments about flame acceleration. In *Proc. International Conference on Fuel-Air Explosions*, pages 77–99. University of Waterloo Press, 1981.

[105] Zhiwu Wang, Weifeng Qin, Lisi Wei, Zixu Zhang, and Yuxiang Hui. Advances on deflagration to detonation transition methods in pulse detonation engines. *Energies*, 18(8):2109, 2025.

[106] E Wintenberger and JE Shepherd. Detonation waves and pulse detonation engines. *California Institute of Technology, Pasadena, CA.[Online]. URL: http://shepherd. caltech. edu/EDL/projects/pde/Ae103-012704. pdf*, 2004.

[107] Piotr Wolański. Detonative propulsion. *Proceedings of the combustion Institute*, 34(1):125–158, 2013.

[108] Ming-hsun Wu, MP Burke, S Ff Son, and RA Yetter. Flame acceleration and the transition to detonation of stoichiometric ethylene/oxygen in microscale tubes. *Proceedings of the Combustion Institute*, 31(2):2429–2436, 2007.

[109] Ming-Hsun Wu and Chan-Yu Wang. Reaction propagation modes in millimeter-scale tubes for ethylene/oxygen mixtures. *Proceedings of the Combustion Institute*, 33(2):2287–2293, 2011.

[110] Matthew X Yao, Jean-Pierre Hickey, and Guillaume Blanquart. Thermoacoustic response of fully compressible counterflow diffusion flames to acoustic perturbations. *Proceedings of the Combustion Institute*, 39(4):4711–4719, 2023.

[111] LJ Zajac and Antoni K Oppenheim. Dynamics of an explosive reaction center. *AIAA Journal*, 9(4):545–553, 1971.

[112] Ya B Zeldovich. *Theory of the propagation limit of quiet flames*. 1941.

[113] Ya B Zeldovich. To the question of energy use of detonation combustion. *Journal of propulsion and power*, 22(3):588–592, 2006.

[114] Ya B Zel'dovich, Vadim Bronislavovich Librovich, Georgii Mikhailovich Makhviladze, and GI Sivashinskil. On the onset of detonation in a nonuniformly heated gas. *Journal of Applied Mechanics and Technical Physics*, 11(2):264–270, 1970.

[115] Bo Zhang and Chunhua Bai. Critical energy of direct detonation initiation in gaseous fuel–oxygen mixtures. *Safety science*, 53:153–159, 2013.

[116] Yunus A. Çengel, Michael A. Boles, and Mehmet Kanoğlu. *Thermodynamics: An Engineering Approach*. McGraw Hill, 10 edition, 2024.